

AD-A120 852

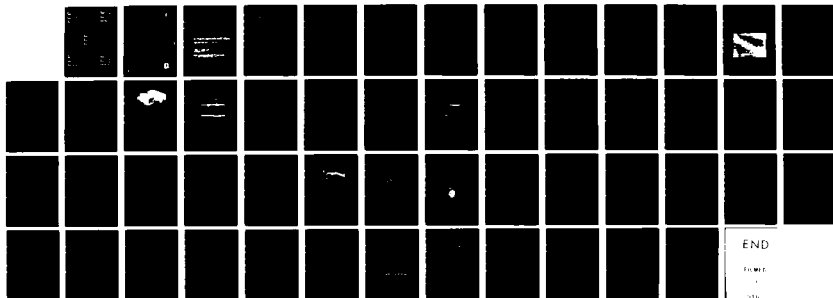
APPLICATION OF THE SATELLITE TRIAXIAL ACCELEROMETER
EXPERIMENT TO ATMOSP. (U) AIR FORCE GEOPHYSICS LAB
HANSCOM AFB MA F A MARCOS ET AL. 04 MAR 82
AFGL-ERP-774

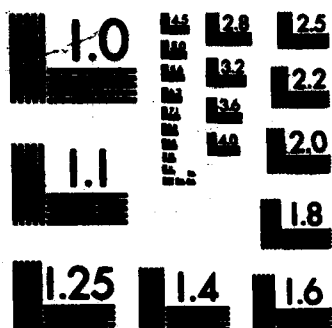
1/1

UNCLASSIFIED

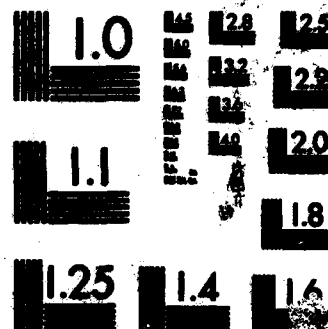
F/G 22/3

NL

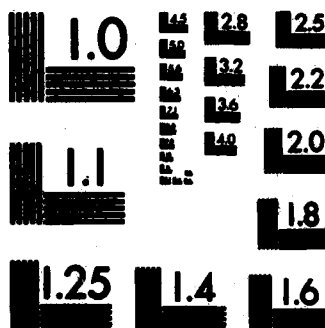




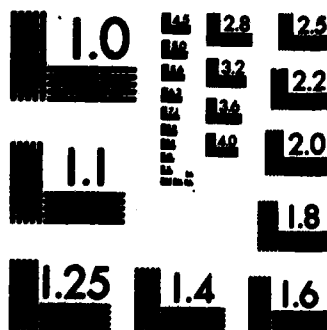
MICROCOPY RESOLUTION TEST CHART
NATIONAL BUREAU OF STANDARDS-1963-A



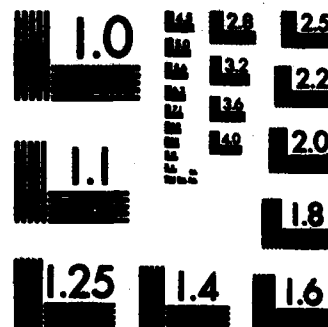
MICROCOPY RESOLUTION TEST CHART
NATIONAL BUREAU OF STANDARDS-1963-A



MICROCOPY RESOLUTION TEST CHART
NATIONAL BUREAU OF STANDARDS-1963-A



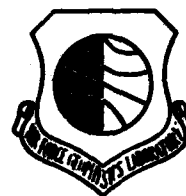
MICROCOPY RESOLUTION TEST CHART
NATIONAL BUREAU OF STANDARDS-1963-A



MICROCOPY RESOLUTION TEST CHART
NATIONAL BUREAU OF STANDARDS-1963-A

12

AFGL-TR-82-0091
ENVIRONMENTAL RESEARCH PAPERS, NO. 774



ADA 120852

Application of the Satellite Triaxial Accelerometer Experiment to Atmospheric Density and Wind Studies

FRANK A. MARCOS
EVERETT R. SWIFT

4 MARCH 1982

DTIC
ELECTE
OCT 29 1982
H

Approved for public release; distribution unlimited.

AERONOMY DIVISION
AIR FORCE GEOPHYSICS LABORATORY
HANSOM AFB, MASSACHUSETTS 01731

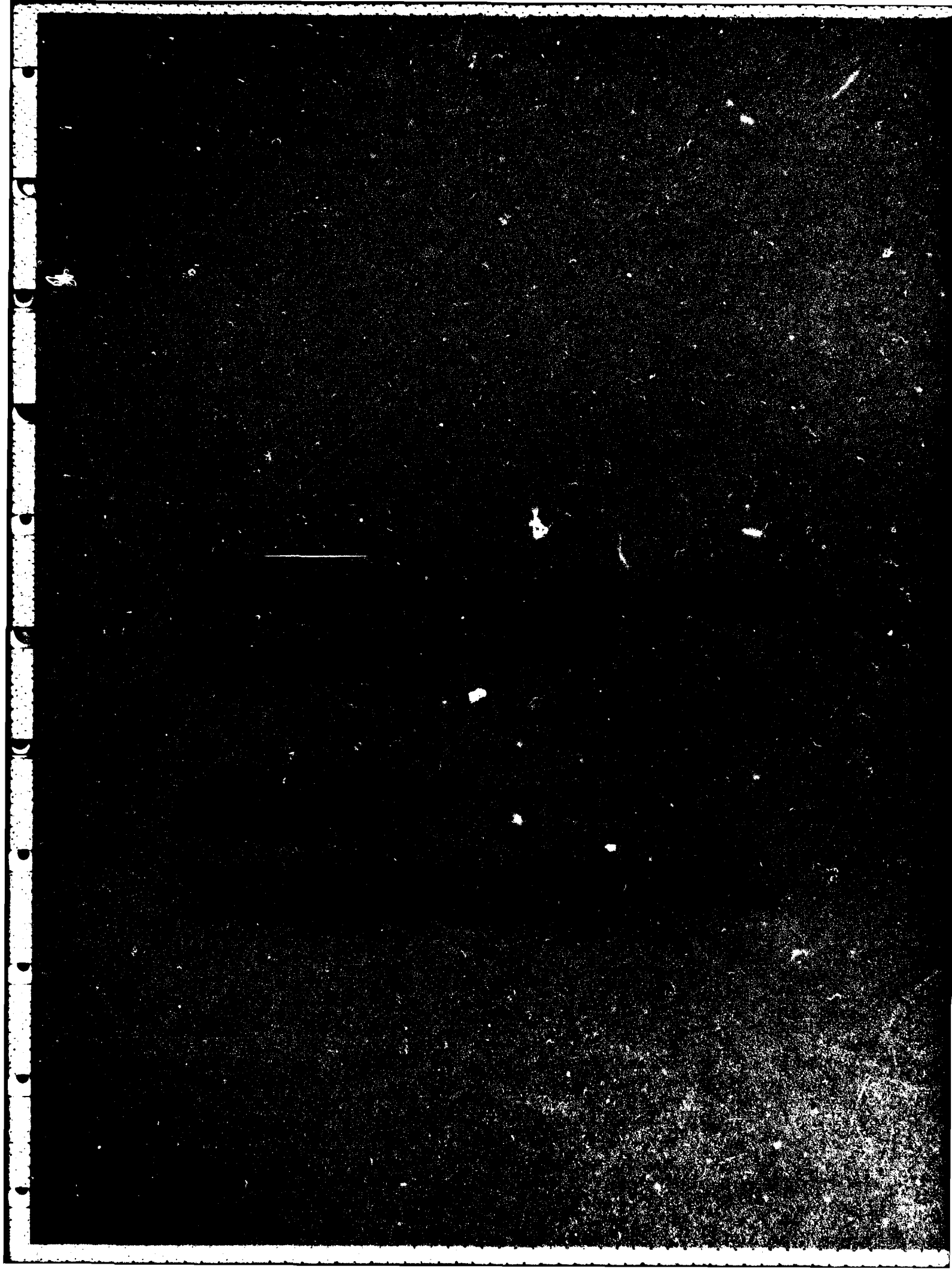
PROJECT 6690

AIR FORCE SYSTEMS COMMAND, USAF



82 10 29 020

DTIC FILE COPY



Unclassified

SECURITY CLASSIFICATION OF THIS PAGE (When Data Entered)

REPORT DOCUMENTATION PAGE		READ INSTRUCTIONS BEFORE COMPLETING FORM
1. REPORT NUMBER AFGL-TR-82-0001	2. GOVT ACCESSION NO. AD-A120852	3. RECIPIENT'S CATALOG NUMBER
4. TITLE (and Subtitle) APPLICATION OF THE SATELLITE TRIAXIAL ACCELEROMETER EXPERIMENT TO ATMOSPHERIC DENSITY AND WIND STUDIES		5. TYPE OF REPORT & PERIOD COVERED Scientific. Interim.
7. AUTHOR(s) Frank A. Marcos Everett R. Swift*		6. PERFORMING ORG. REPORT NUMBER ERP, No. 774
8. PERFORMING ORGANIZATION NAME AND ADDRESS Air Force Geophysics Laboratory (LKB) Hanscom AFB Massachusetts 01731		9. CONTRACT OR GRANT NUMBER(s)
11. CONTROLLING OFFICE NAME AND ADDRESS Air Force Geophysics Laboratory (LKB) Hanscom AFB Massachusetts 01731		10. PROGRAM ELEMENT, PROJECT, TASK AREA & WORK UNIT NUMBERS PE 82101F 66900408
14. MONITORING AGENCY NAME & ADDRESS (if different from Controlling Office)		12. REPORT DATE 4 March 1982
		13. NUMBER OF PAGES 53
		15. SECURITY CLASS. (of this report) Unclassified
		15a. DECLASSIFICATION/DOWNGRADING SCHEDULE
16. DISTRIBUTION STATEMENT (of this Report) Approved for public release; distribution unlimited.		
17. DISTRIBUTION STATEMENT (of the abstract entered in Block 20, if different from Report)		
18. SUPPLEMENTARY NOTES *Naval Surface Weapons Center, Dahlgren, Virginia		
19. KEY WORDS (Continue on reverse side if necessary and identify by block number) Satellites Upper atmosphere winds Accelerometers Thermospheric density Aerodynamic drag Atmospheric density		
20. ABSTRACT (Continue on reverse side if necessary and identify by block number) → A new satellite triaxial accelerometer system has been developed. This instrument has been flight-tested on three-axis stabilized satellites and has demonstrated the capability to accurately measure accelerations in the satellite's in-track, cross-track, and radial directions. The in-track data provide direct determination of atmospheric density. These data, obtained during a period of high solar flux, supplement the extensive set of measurements obtained by other accelerometer experiments during low solar flux conditions. The cross-track and radial results permit, for the first time, large-scale		

DD FORM 1 JAN 73 1473 EDITION OF 1 NOV 65 IS OBSOLETE

Unclassified

SECURITY CLASSIFICATION OF THIS PAGE (When Data Entered)

Unclassified

SECURITY CLASSIFICATION OF THIS PAGE(When Data Entered)

20. Abstract (Continued)

measurements of the zonal and, possibly, radial components of neutral atmospheric winds. These simultaneous wind and density data provide an extremely valuable input for the understanding of dynamic processes in the atmosphere and for the improvement of atmospheric models.

Unclassified

SECURITY CLASSIFICATION OF THIS PAGE(When Data Entered)

Preface

Funds to initiate the accelerometer development were provided by the AFGL In-House Independent Laboratory Director's Fund. Murray Meldrum and William Lange, Bell Aerospace Textron, were principal investigators for instrument fabrication under AF Contract F19628-74-C-0114.

At NSWC Linda Lynch and Becky Boyer were responsible for daily quick-look data analysis and generation of raw data tapes for AFGL. Additional assistance in data quality analysis was provided by Carol Branch. The data processing and plotting software was generated by Allen Fisher, Ling Szeto, and Dee Batayte.

Processing of density and wind data was accomplished by R. W. Fioretti, A. J. Mazzella, Jr., and R. Leong of RDP, Inc. under AF Contract F19628-76-C-0244. Material for Figures 14 and 17b was generated by Edward Robinson (SUWA). Dorothy Gillette and Sammy Chan assisted in various aspects of data presentation. Margaret Anderson and Stephanie Furlow typed the numerous drafts and final manuscript. Critical technical comments were provided by K. S. W. Champion and J. M. Forbes.



Accession For	
NTIS GRA&I	<input checked="" type="checkbox"/>
DTIC TAB	<input type="checkbox"/>
Unannounced	<input type="checkbox"/>
Justification	
By	
Distribution/	
Availability Codes	
Dist	Avail and/or Special
A	

Contents

1. INTRODUCTION	9
2. EXPERIMENT DESCRIPTION	10
3. ORBITAL FLIGHT DATA	15
4. DATA ANALYSIS	23
5. GEOPHYSICAL STUDIES	29
5.1 Relation of Data to Atmospheric Studies	30
5.1.1 Neutral Atmospheric Heating and Dynamics	
Overview	30
5.1.2 Orbital Data Collection	33
5.2 Atmospheric Density Results	35
5.2.1 Solar Flux Effects	36
5.2.2 Geomagnetic Activity Effects	37
5.2.3 Wave Structures	38
5.3 Neutral Atmospheric Wind Results	41
6. CONCLUSIONS	48
REFERENCES	50

Illustrations

1. Instrument Mechanical Assembly	11
2. Block Diagram of Y- (or X-) Axis Force Rebalance Loop	12

Illustrations

3. Block Diagram of Z-Axis Force Rebalance Loop	13
4. Accelerometer Flight Package	15
5. Raw Data for Test Flight	16
6. Proof-Mass Housing Geometry	18
7. Raw Data for One Orbit, Day 79094	20
8. Bias Drift Data for One Day, Day 79108	22
9. Filtered Data for One Orbit, Day 79094	24
10. X-, Y-, and Z-axis Bias Values, Days 79079-79100	26
11. Drag Coefficients for X, Y, and Z Directions	28
12. Diagram of Earth's Magnetosphere	32
13. Heat Sources for the Upper Atmosphere	33
14. Intersection of Satellite Tracks for One Day with Northern Hemisphere Auroral Zone	34
15. Atmospheric Density as a Function of Altitude, Latitude, and Local Time	35
16. Atmospheric Density as a Function of Solar Flux	37
17a. Atmospheric Density Response to a Geomagnetic Storm	39
17b. Model Prediction of Density Response to a Geomagnetic Storm	40
18. Wave Structure in an Atmospheric Density Profile	42
19. Accelerometer Cross-axis Angle of Attack vs Geographic Latitude	44
20. Cross-axis Acceleration Data During a Period of Moderately Low Geomagnetic Activity	44
21. Horizontal Wind Velocities During a Period of Moderately Low Geomagnetic Activity	45
22. Cross-axis Acceleration Data During a Period of High Geomagnetic Activity	46
23. Horizontal Wind Velocities During a Period of High Geomagnetic Activity	46
24a. Radial-axis Acceleration Data During a Period of Moderately Low Geomagnetic Activity	47
24b. Radial-axis Acceleration Data During a Period of High Geomagnetic Activity	48

Tables

1. Single-Axis Accelerometer (MESA) Flight History	10
2. Accelerometer Sensitivity Ranges	14
3. Instrument Improvement Summary	21

Application of the Satellite Triaxial Accelerometer Experiment to Atmospheric Density and Wind Studies

1. INTRODUCTION

A single-axis accelerometer system, MESA (Miniature Electrostatic Accelerometer), has been flown successfully by the Air Force Geophysics Laboratory (AFGL) on eight satellites. Table 1 lists the spacecraft, their launch dates and lifetimes. Except for S3-1 and S3-4, all flights utilized three single-axis sensors mounted orthogonally to achieve a triaxial sensing capability. The resulting package typically weighed 10 kg and consumed about 20 W of power. The accelerometer proved to be extremely accurate and reliable on all missions. For example, on the Atmosphere Explorer-C (AE-C) satellite, accelerations were measured over a five-year period. During its first year of operation, with the spacecraft in a highly elliptical orbit, the instrument was used to measure density, orbit-adjust thrusts, and vehicle motions. For about the next four years AE-C was in a circular orbit too high for accurate density data to be obtained. However, the instrument was operated as required for monitoring of thrusts and vehicle motions by NASA to control the satellite. During the last few weeks of the AE-C lifetime, when its altitude was below 250 km, density measurements were again obtained. The AE-E triaxial accelerometer, launched in 1975, has been utilized in a similar manner, and reentry data were obtained during June 1981. Marcos et al¹ have

(Received for publication 2 March 1982)

1. Marcos, F.A., McInerney, R.E., and Fioretti, R.W. (1978) Variability of the Lower Thermosphere Determined From Satellite Accelerometer Data, AFGL, Hanscom AFB, Mass., AFGL-TR-78-0134, ADA 058982.

Table 1. Single-Axis Accelerometer (MESA) Flight History

Satellite	Launch Date	Lifetime
Cannon Ball 1	July 1968	39 days
OV1-15	July 1968	4 months
Cannon Ball 2	Aug. 1971	1 1/2 years*
Atmosphere Explorer-C	Dec. 1973	5 years
S3-1	Sep. 1974	6 months
Atmosphere Explorer-D	Oct. 1975	1 1/2 years**
Atmosphere Explorer-E	Dec. 1975	5 years
S3-4	Mar. 1978	6 months***

*Spacecraft power failure after 80 days terminated satellite operation.

**Spacecraft power failure after 90 days terminated satellite operation.

***Motor used to rotate accelerometer failed after five months, terminated instrument operation.

summarized results from four experiments (AE-C, AE-D, AE-E, and S3-1). Further scientific results from the MESA flights are referenced at appropriate points in the text.

During 1975, an Air Force contract using Laboratory Director's Funds was awarded to Bell Aerospace, Textron, to develop an instrument with a single proof mass sensitive along three orthogonal axes. The goals of this effort were to achieve a significant reduction in cost as well as in size, weight, and power while maintaining the accuracy and reliability of the flight-proven MESA system. This report describes the accelerometer experiment, and provides a brief survey of the density and wind measurements and their application to developing improved models of the atmosphere.

2. EXPERIMENT DESCRIPTION

The new Satellite Electrostatic Triaxial Accelerometer (SETA) design is based on the flight-proven single-axis MESA. The MESA utilizes a proof mass in the shape of a flanged hollow cylinder. This proof mass is suspended electrostatically along its radial axes. It is force-rebalanced electrostatically along its longitudinal or sensitive axis. A complete description of the MESA instrument that was

flown successfully on three Atmosphere Explorer satellites has been given by Champion and Marcos.² To develop a triaxial sensing capability the suspension system was modified by instrumenting both radial axes with precision constraint loops. A brief description is given in the following paragraphs.

Figure 1 shows the mechanical assembly of the instrument. The one gram proof mass, in the center of the assembly, is constrained in all three axes by means of electrostatic forces generated by electrodes. There are a total of 14 electrodes, three on each of the forcer rings facing both sides of the flange and eight on the carrier cylinder facing the inside of the proof-mass cylinder. The Z axis is along the axial centerline of the proof-mass cylinder as in the single-axis instrument. The X and Y axes are perpendicular to the cylinder and are each defined by the four pairs of electrodes on the carrier. The proof-mass cylinder



Figure 1. Instrument Mechanical Assembly

2. Champion, K.S.W., and Marcos, F.A. (1973) The triaxial accelerometer system on Atmosphere Explorer, Radio Sci. 8:197.

is 0.025-cm thick and its flange is 0.0375-cm thick. The spacer has a thickness of 0.056 cm. The gap between the flange and each Z-axis forcer electrode is 0.0089 cm. Between the X- and Y-axes carrier electrodes and the inside of the proof-mass cylinder the gap is 0.0033 cm.

Accelerations along the Z axis are measured by the set of six electrodes facing the flange. The X and Y axes are each controlled by two pairs of electrodes on opposite sides of the carrier. The X and Y axes constraintment systems are identical, each using two constraintment circuits to prevent rotation in two axes. The Z axis requires only a single circuit. The proof mass is not constrained against rotation about the cylinder axis. Figures 2 and 3 are block diagrams, for the Y (or X) and Z axes respectively, of the constraint loop connections to the electrodes within the mechanical assembly. Measurement of acceleration is accomplished by sensing motion of the proof mass with respect to the instrument case. An electrostatic force is then generated on the appropriate electrodes to restore the proof mass to its null or zero input position. The restoring force is generated by a dc voltage proportional to input acceleration. This voltage is fed to a precision A/D converter. The output of the instrument consists of a digital pulse rate proportional to the input acceleration.

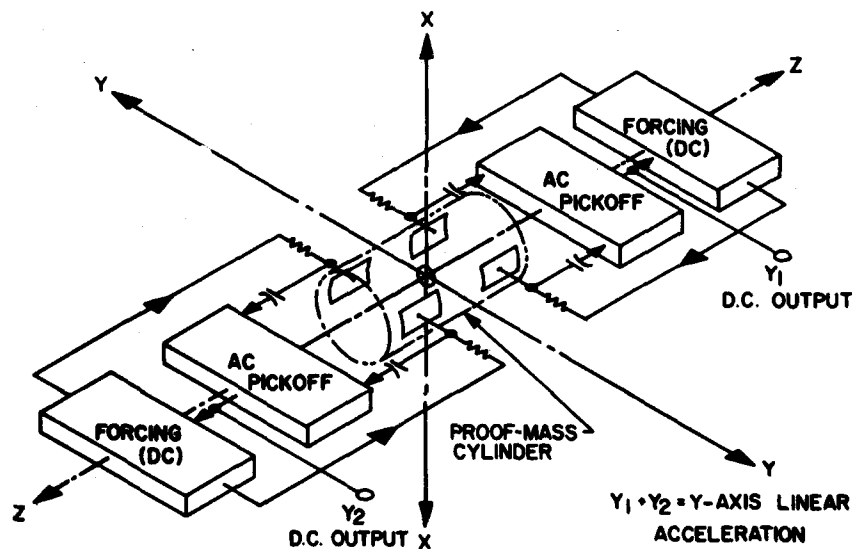


Figure 2. Block Diagram of Y- (or X-) Axis Force Rebalance Loop

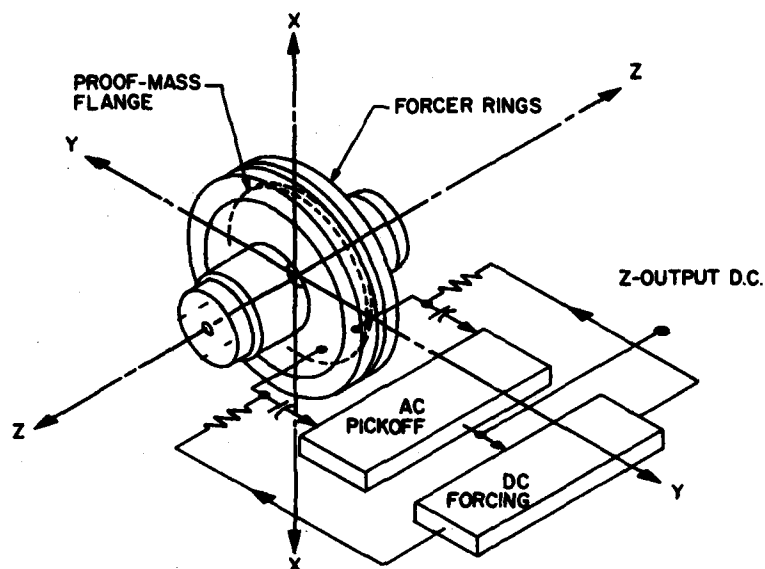


Figure 3. Block Diagram of Z-Axis Force Rebalance Loop

The magnitude of the accelerations that must be measured varies from $1.2 \times 10^{-2} g$ for a maximum orbit-adjust engine thrust down to approximately $1 \times 10^{-8} g$ for high-altitude drag data. Three sensitivity ranges are used for each axis to cover this measurement interval. These ranges are selected automatically during flight. The scaling is selected independently for each axis. The nominal maximum g level for each constraint range is given in Table 2 for a test flight unit and the operational flight unit.

The instrument maximum pulse rate output representing full scale in a positive or negative direction is 15 kHz. The digital accumulator is a bidirectional or up-down counter that stores the incoming pulses for a given sampling time and then provides three output words in serial form. This output word represents the average acceleration input over the 2.045-sec sample period. Instrument temperature is monitored as an analog word once every 114.5 sec by a thermistor placed near the proof mass. Based upon this pulse rate and sample time, accelerations as low as $2 \times 10^{-9} g$ can be sensed on the most sensitive scale of the operational unit.

Table 2. Accelerometer Sensitivity Ranges

	Test/Future Flights	Operational Flight
X, Y Axes		
Ranges A	15000 μ g	6000 μ g
B	1500	600
C	300	60
Z Axis		
Ranges A	15000 μ g	15000 μ g
B	1500	900
C	150	60

An analysis of satellite mechanical vibrations induced by the attitude control thrusters was performed.^{3,4} These studies indicated noise peaks at several frequencies. Electronic filtering was added to the accelerometer to minimize the effects of the noise accelerations. The bandwidth response is as follows: 1.0 at dc, 0.997 at 0.1 Hz, 0.5 at 0.25 Hz, and 0.003 at 6.0 Hz.

Accelerometer scale factor calibration is achieved by introducing a fraction of the earth's $1g$ field into the sensitive axis. This is accomplished by tilting the sensitive axis by a known angle from the horizontal, zero input position. Accuracy of the scale factor measurement is limited by the ability to generate and maintain very small angular displacements. To achieve ground calibration data at very low input levels a laser interferometer is used. It has a resolution capability of 0.02 arc sec ($10^{-7}g$). The scale factor is a function of temperature due mainly to the expansion and contraction of mechanical parts. Temperature calibrations were performed in the range between 70° and 120°F. The calibration involved repeated measurements with emphasis on the Z axis and its most sensitive scale (C-range of Table 2). Standard deviations of the C range calibration data were typically 0.1 μ g. Scale factor temperature coefficients were of the order of 0.1 percent/°F.

The accelerometer flight hardware is shown in Figure 4. The instrument weighs 4.6 kg, and has the dimensions 8.9 × 12.7 × 29.2 cm. Maximum power

3. Counts, J. (1975) Effects of Flexible Solar Arrays on Sensed Accelerations in a Rigid Spacecraft, VPI-E-75-13, Virginia Polytechnic Institute and State University, Blacksburg, Virginia.
4. Butler, T.A. (1977) Effect of Attitude Control Thruster-Induced Structural Vibrations on Sensed Accelerations of a Space Vehicle, Los Alamos Scientific Laboratories, Informal Report LA-6965-MS, Los Alamos, N.M.



Figure 4. Accelerometer Flight Package

consumption is 11.7 W. The accelerometer is mounted with its Z axis aligned with the satellite in-track direction, the Y axis along the earth's radial direction, and the X axis in the cross-track direction. Due to satellite physical limitations the instrument was mounted below, to one side, and forward of the center of gravity.

The telemetry data tapes were processed at NSWC for decommutation and time-tagging. Tapes containing only time, accelerometer raw data, and temperature were then prepared and shipped routinely to AFGL for processing to derive density and wind data. Experiment operation was monitored at NSWC by preparing plots of acceleration vs time on a routine basis.

3. ORBITAL FLIGHT DATA

An orbital accelerometer flight test was conducted. After turn-on the automatic range circuit functioned normally and put all three axes into their most sensitive range. This indicated that the preflight estimates of the orbital acceleration environment and instrument response characteristics were accurate. Data obtained on all three axes during one orbit are shown in Figure 5. The top frame shows the accelerations sensed in the along-track (Z) direction. The next two frames show accelerations measured in the radial (Y) and cross-track (X) directions, respectively. The bottom frame shows the temperature ($^{\circ}\text{F}$) measured inside the proof-mass housing. A typical curve of the Z-axis drag acceleration vs time would vary at the orbital rate and have its maximum value at the time the

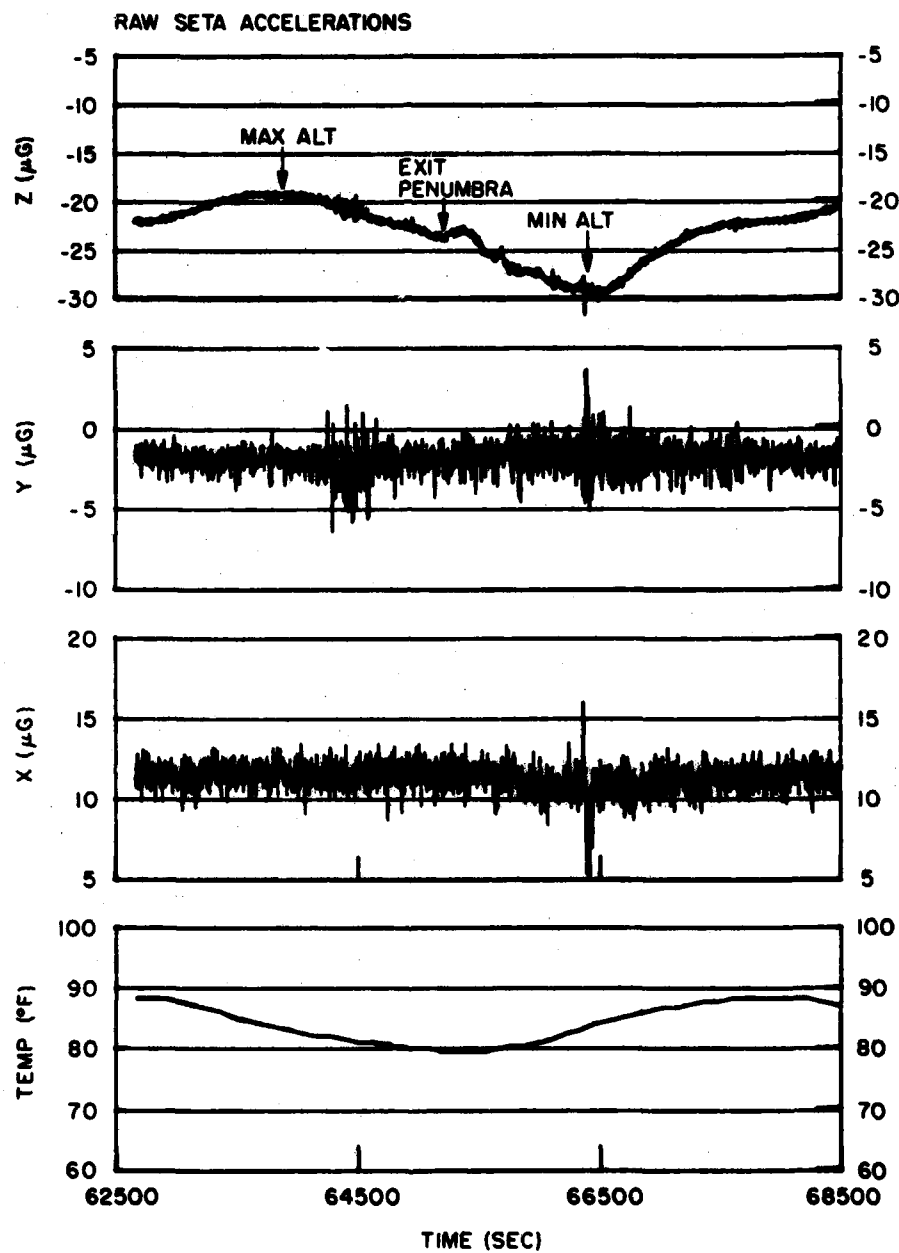


Figure 5. Raw Data for Test Flight

satellite is at its lowest altitude (where the density is highest). Drag accelerations are sensed with a negative polarity for this experiment. Hence, maximum densities correspond to more negative acceleration values and minimum densities correspond to less negative acceleration values. For the data in Figure 5, the instrument bias shifts the curve downward for the Z axis. The instrument successfully provided measurements on all three axes. Several anomalies were observed and are discussed below.

Examination of the in-track data in Figure 5 shows general characteristics of a drag profile with the largest drag near minimum altitude. However the results are dominated by an opposite polarity spike peaking at 65400 sec GMT. This spike has a 2- μ g amplitude and about 500-sec duration. It was subsequently determined that this most significant deviation from the anticipated drag profile was caused by the large heat input experienced when the instrument was exposed to solar radiation. Onset occurred when the satellite exited penumbra. At this time the instrument temperature begins to increase. The result of this temperature increase is to cause an apparent decrease in sensed acceleration. Termination of the spike occurred when the vehicle pitched down sufficiently to shade the instrument. Further study revealed that the accelerometer was responding in a complicated manner to thermal variations throughout the orbit. Other anomalies found in the data were the following:

(a) Bias values were initially high on all three axes. The data in Figure 5 shows a bias of approximately -20 μ g, -2 μ g, and +12 μ g for the Z, Y, and X axes respectively. Initial values of -15 μ g, -150 μ g, and +125 μ g respectively, approached the values in Figure 5 in about one day.

(b) The approximately 2- μ g peak-to-peak noise on the radial and cross-track axes precluded obtaining useful data from them. The noise in these axes was not satisfactorily explained. However, no evidence of a feature corresponding to the Z-axis spike was found.

Several orbital maneuvers were performed to study further the instrument behavior. These tests showed that all three axes were properly responding to atmospheric density and to vehicle dynamics. However, because of the contamination of the data by the temperature anomaly, it was determined that geophysical information could not be extracted with sufficient accuracy to extend present modeling efforts.

The contractor (Bell Aerospace Textron) determined that the high initial bias values were due to charge build-up on the electrode carrier dielectrics. They also suggested that increasing the sensitivity would result in lower steady-state bias values. The initial scaling had been limited to the maximum sensitivity the contractor recommended. They now felt, based on flight experience, that the sensitivity could be improved.

The cause of the temperature anomaly was accidentally discovered during tests of the next flight unit at Bell Aerospace Textron. It was found that application of heat to the proof-mass housing caused a jump in the Z-axis output. Flexing of the thin housing walls in response to temperature variations created a flow of air out of a vent hole in the electrode carrier and against the cylinder flange that detects Z-axis motions. The geometry of the proof-mass housing area and the air flow are shown in Figure 6. This diagram also shows that the X and Y axes were apparently not affected since the flow is perpendicular to them. On the single-axis instruments the vent hole was placed symmetrically with respect to the flange on the stainless steel spacer ring. In the development of the three-axis system the hole could not be drilled through the thin (0.056 cm) spacer ring, now made of ceramic, hence it was placed on the electrode carrier.

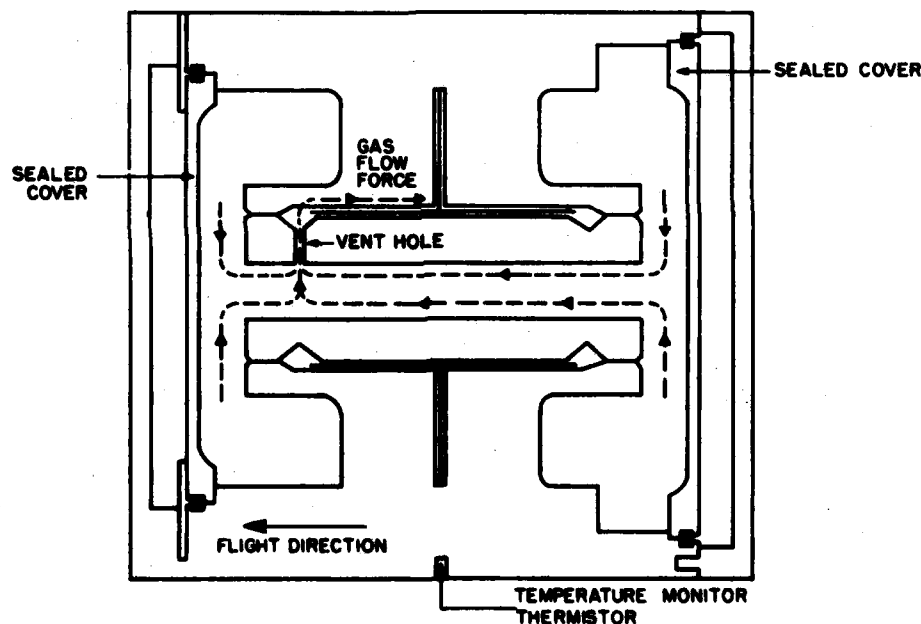


Figure 6. Proof-Mass Housing Geometry

Based on flight data and the testing at Bell Aerospace Textron, the following changes were incorporated into the next flight unit:

- (a) A second vent hole was drilled into the electrode carrier. It was placed symmetrically opposite the first hole with respect to the proof-mass flange.

(b) A temperature controller was added to eliminate the need for a temperature-dependent scale factor correction to the flight data. This controller, designed to operate at $105^{\circ}\text{F} \pm 0.3^{\circ}\text{F}$ consisted of two 1.5-W heaters. A section was added at each end of the housing to accommodate the heaters.

(c) The sensitivity was increased for all three axes as shown in the data of Table 2. This was done to reduce the bias as well as to achieve more accurate measurements.

(d) Low noise preamplifiers were used to reduce noise in the cross axes.

This modified instrument was operated during 1979. Early flight data indicated that the revisions put into this unit resulted in extremely accurate acceleration measurements on all three axes. Results are shown for one orbit in Figure 7. This format is identical to that of Figure 5. The Z-axis data show a drag profile with maximum value at minimum altitude and a $7\text{-}\mu\text{g}$ amplitude. There is no evidence of the spike or other anomalous temperature effects. The Y-axis noise is sufficiently low that the orbit-attitude pulses, more frequent near perigee, are distinguishable. On the X-axis a $1\text{-}\mu\text{g}$ peak-to-peak modulation is due to atmospheric wind motions. Stabilization of the instrument operating temperature at $110^{\circ}\text{F} \pm 0.3^{\circ}\text{F}$ occurred within one hour after instrument turn-on. Table 3 summarizes the improvements in sensitivity, noise reduction, and bias achieved with this flight. Applications of these high accuracy, high resolution measurements are discussed in Section 5.

Normal operation continued for about 22 days. Stabilization of the temperature 5°F above the value obtained in ground tests was attributed by Bell Aerospace Textron to the effect of convection of heat away from the proof-mass housing during ground tests. Since they had not considered this before launch, data were reduced by using a linear extrapolation of the calibration data.

Instrument performance began to degrade after about 22 days of operation. The problem initially showed up as a drift in the Y-axis bias. The other two axes were affected but to a lesser extent. This drift increased with time on all three axes. Figure 8 shows a plot of the response of all three axes after about one week of anomalous operation. The sudden shifts toward a zero bias were frequently correlated with vehicle noise. This problem persisted throughout the flight. Events such as orbit-adjusts and instrument turn-off/turn-ons lowered the bias and its drift rate.

Analyses of characteristics of the anomalous instrument operations were provided to the contractor but they were unable to account for these phenomena. Tests of various electrical components were performed but the bias drift could not be reproduced. A possible problem discovered during testing was that the two sealed covers on the ends of the proof-mass housing could be assuming a potential. This would occur if they became electrically isolated from the case. Tests of one

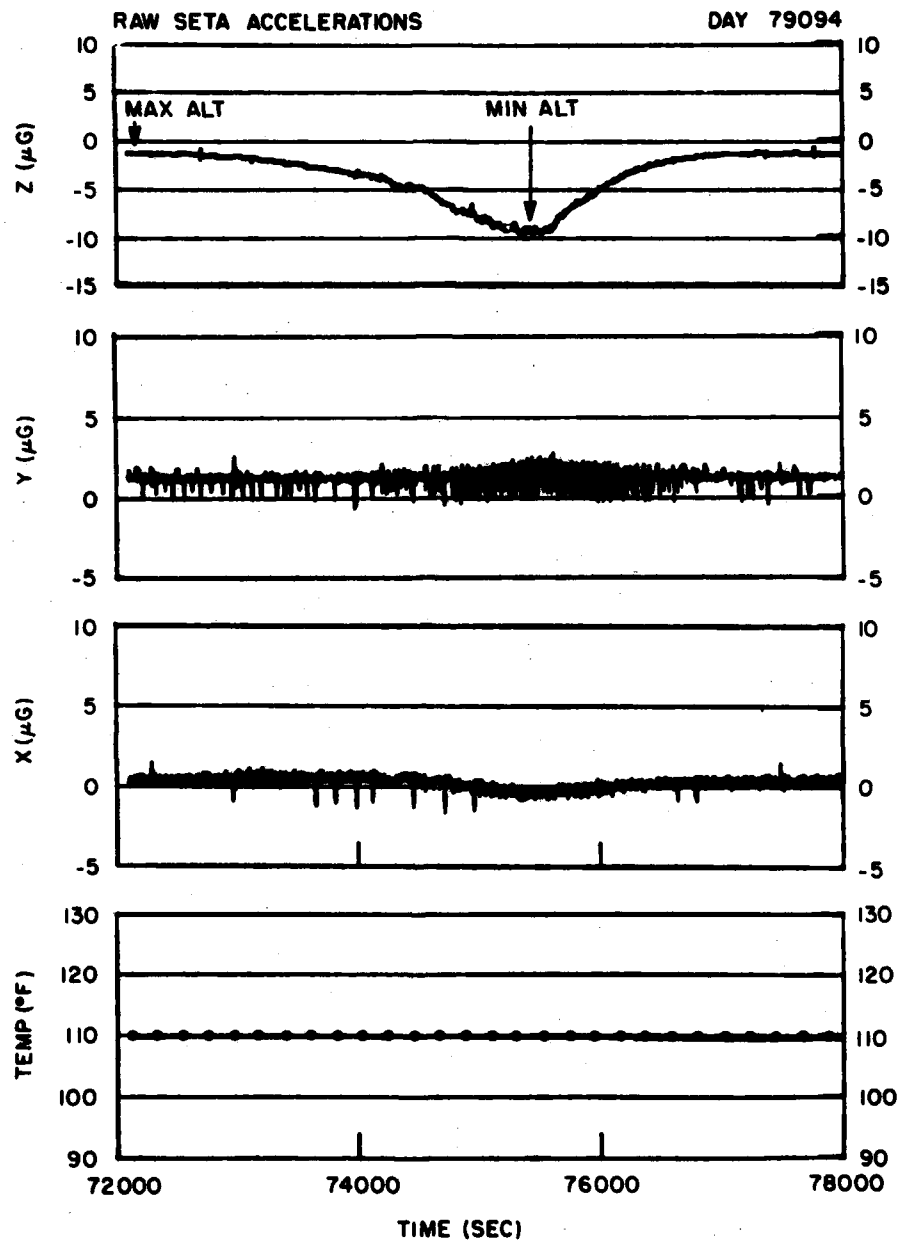


Figure 7. Raw Data for One Orbit, Day 79094

Table 3. Instrument Improvement Summary

	Test Flight	Operational Flight
Temperature Anomaly		
Amplitude	2 μ g	none
Duration	500 sec	none
Noise (μg; peak-to-peak)		
Z-axis	0.4 μ g	0.2 μ g
X-axis	2.2	0.8
Y-axis	2.2	0.5
Bias (μg)		
Z initial	-15 μ g	+6 μ g
final	-20	+2
X initial	+120	+11
final	+12	+1
Y initial	-125	-8
final	-2	+3
Sensitivity (Maximum full scale)		
Z	150 μ g	60 μ g
Y	300	60
X	300	60

pre-flight unit were performed. An open circuit condition was found between the case and one cover. The cause was attributed to failure of the epoxy seal induced by internal pressure or continuous flexing due to heater cycling. If this occurred in orbit the accelerometer output could exhibit the observed erratic behavior. Another potential problem found was that interference occurred between the voltage regulator switching frequency at various line voltages and the proof-mass suspension frequencies (60, 80, and 100 MHz for X, Y, and Z respectively). This interference results in a step change in output with no subsequent time variations. Hence this possible problem is distinct from the bias drift anomaly.

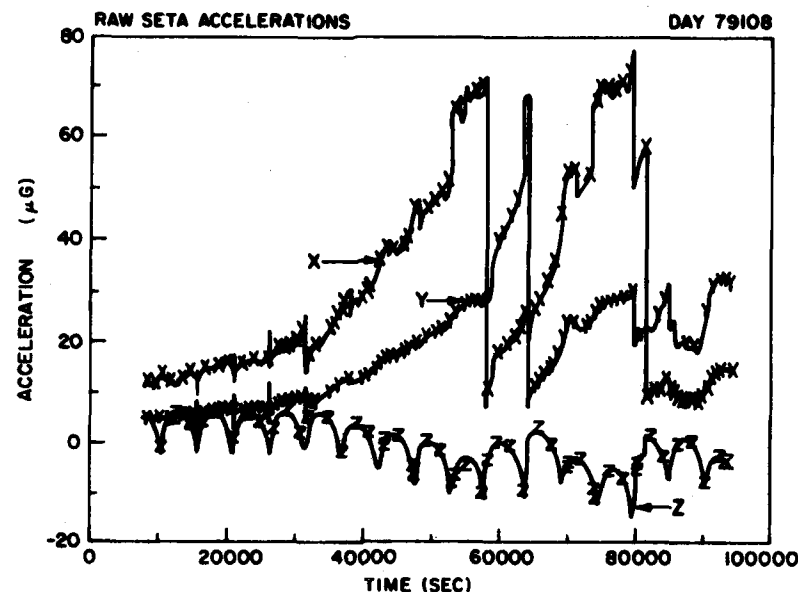


Figure 8. Bias Drift Data for One Day, Day 79108

Since the test flight did not exhibit a bias problem, possible effects of the four changes incorporated after this flight were examined. The second vent hole and the low noise pre-amplifiers were determined to be unrelated to the problem. The increase in C-range sensitivity was suspected as a possible cause of an instability in the instrument response to acceleration impulses, and the duty-cycle heaters were suspected as a possible cause of intermittent electrical interference. Pre-flight tests of the instrument did not reveal any anomalies. However, because of the limitations of testing in earth's one-g environment and the possibility of a component degradation in orbit leading to marginal instrument performance, the latter two changes are not assumed to be unrelated to the bias drift problem.

As a result of the above tests and analyses of flight data, it was decided that the following changes would be implemented into any future flight units:

- (a) Ground the cover to the case.
- (b) Replace the switching (voltage) regulator with a nonswitching type.
- (c) Use the same sensitivity levels as those on the test flight on all three axes.
- (d) Disconnect the heaters internally.

4. DATA ANALYSIS

The accelerometer output contains contributions related to vehicle dynamics and instrument operating characteristics as well as those due to aerodynamic drag and winds. The vehicle dynamic accelerations (\vec{a}_v) are mainly those due to spacecraft vibrations induced by the attitude control system (discussed in Section 2). Centripetal acceleration and the gravity gradient effect, each of the order of $0.32 \mu g$ but oppositely directed, provide a negligible ($<0.01 \mu g$) resultant dynamic acceleration in the along-track axis. Also, the radial-axis data contain essentially constant contribution due to the gravity gradient acceleration ($-0.08 \mu g$). Extraneous accelerometer outputs consist of a bias (\vec{a}_B) and random noise (\vec{a}_N). With the centripetal and gravity gradient accelerations incorporated as part of the bias term, the average accelerometer output over the 2.045-sec sample time (a_T) is then represented by:

$$a_{Ti} = a_{Di} + a_{vi} + a_{Bi} + a_{Ni} \quad (1)$$

where $i = X, Y, Z$ since the various acceleration sources can be different along each axis. The aerodynamic component is derived using Eq. (1) in the form:

$$a_{Di} = a_{Ti} - \{a_{vi} + a_{Bi} + a_{Ni}\}$$

Numerical filtering techniques (for example, Noonan et al⁵) are used to remove the high frequency components of \vec{a}_T due to satellite dynamics (\vec{a}_v) and instrument noise (\vec{a}_N). Figure 9 shows the result of applying a filter passing only frequencies less than 0.01 Hz to the data of Figure 7. The data are offset from zero since filtering does not remove the nearly steady-state bias. Since the in-track accelerometer axis senses aerodynamic drag throughout the orbit, bias cannot be directly deduced by the Z-axis accelerometer output at apogee. A bias value is estimated for each orbit essentially by subtracting a drag acceleration based on a model density value⁶ from the filtered accelerometer output at maximum altitude. This density typically corresponds to a drag value of $0.4 \mu g$. For the cross-track and radial axes, aerodynamic accelerations are negligible at this altitude. However bias determination is complicated by low frequency noise (<0.01 Hz) with an

5. Noonan, J. P., Fioretti, R. W., and Hass, B. (1975) Digital Filtering Analysis Applied to the Atmosphere Explorer-C Satellite MESA Accelerometer Data, AFCHL-TR-75-0293, ADA 015785.

6. Jacchia, L. G. (1971) Revised Static Models of the Thermosphere and Exosphere With Empirical Temperature Profiles, Spec. Rep. 332, Smithsonian Astrophys. Observ., Cambridge, Mass.

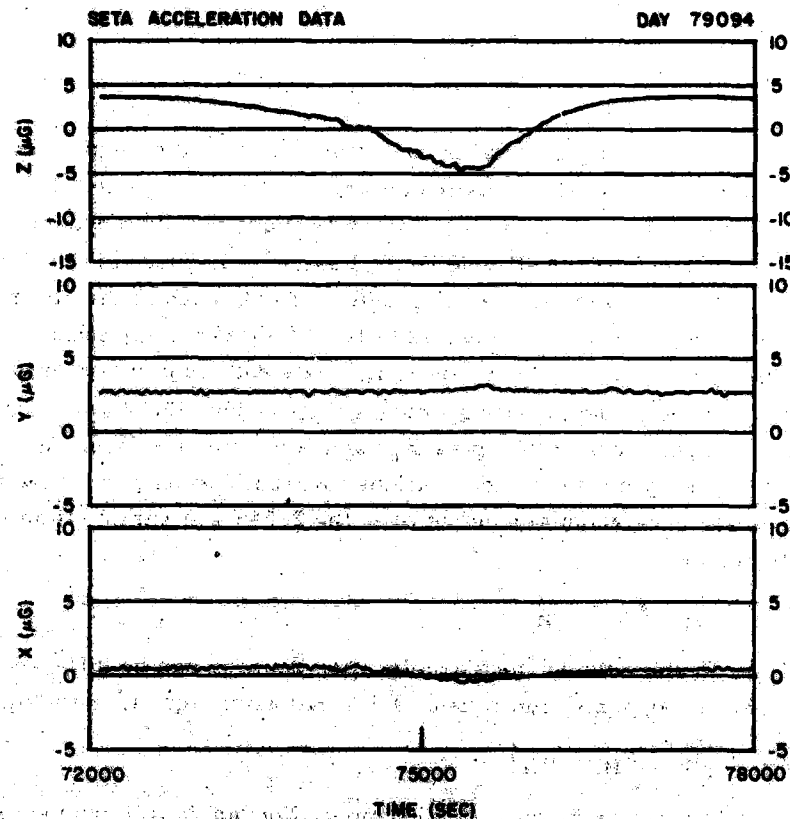


Figure 9. Filtered Data for One Orbit, Day 79094

amplitude of about $0.04 \mu\text{g}$ in the Z axis and $0.08 \mu\text{g}$ in the X and Y axes. The source of the noise appears to be satellite vibration with the measured spectrum affected by aliasing. Two additional steps were taken to obtain an accurate bias estimate. First, a 500-sec bias average centered on maximum altitude was used instead of just the maximum altitude value. Second, the average bias estimates for all data during 22 days of normal operation were fit with an expression of the form:

$$a_D(t) = K_1 + K_2 \exp(K_3 t) + K_4 \exp(K_5 t) \quad (2)$$

where t = time in days from day 79077.00, and the coefficients for each axis are:

	X	Y	Z
K_1	-147.3229×10^{-6}	2.5344×10^{-6}	4.4670×10^{-6}
K_2	9.1053×10^{-6}	-6.4650×10^{-6}	-1.4235×10^{-6}
K_3	-1.6944	-1.5259	-0.7675
K_4	147.7283×10^{-6}	0.4453×10^{-6}	-1.8088×10^{-6}
K_5	-0.1463×10^{-4}	0.0583×10^{-6}	-0.1027

Results are shown in Figure 10 for each axis. The solid-line fit to the individual points represents the bias.

The equations used for the determination of atmospheric density and wind velocities are:

$$a_{Di} = \frac{A_{ref}}{2m} C_i \rho V^2 \quad (3)$$

where

$i = X, Y, Z$

a_{Di} = drag acceleration

A_{ref} = satellite frontal area

m = satellite mass

ρ = atmospheric density

\vec{V} = atmospheric mass velocity relative to the satellite

$$\vec{V} = -\vec{V}_G + \vec{V}_A + \vec{V}_W \quad (4)$$

with \vec{V}_G , \vec{V}_A , and \vec{V}_W representing respectively, inertial satellite velocity, the atmospheric rotation velocity (assumed equal to earth's rotation velocity) and the neutral wind velocity

C_i = drag coefficients: $C_i = C_i(V_X, V_Y, V_Z)$.

The results of Sentman⁷ are used to describe the components of the satellite drag coefficient. In this formulation the equation for the component in a particular direction of the total force on an element of area is given by:

7. Sentman, L.H. (1961) Free Molecular Flow Theory and Its Application to the Determination of Aerodynamic Forces, LMSC-448514, Lockheed Missiles and Space Co., Sunnyvale, Calif.

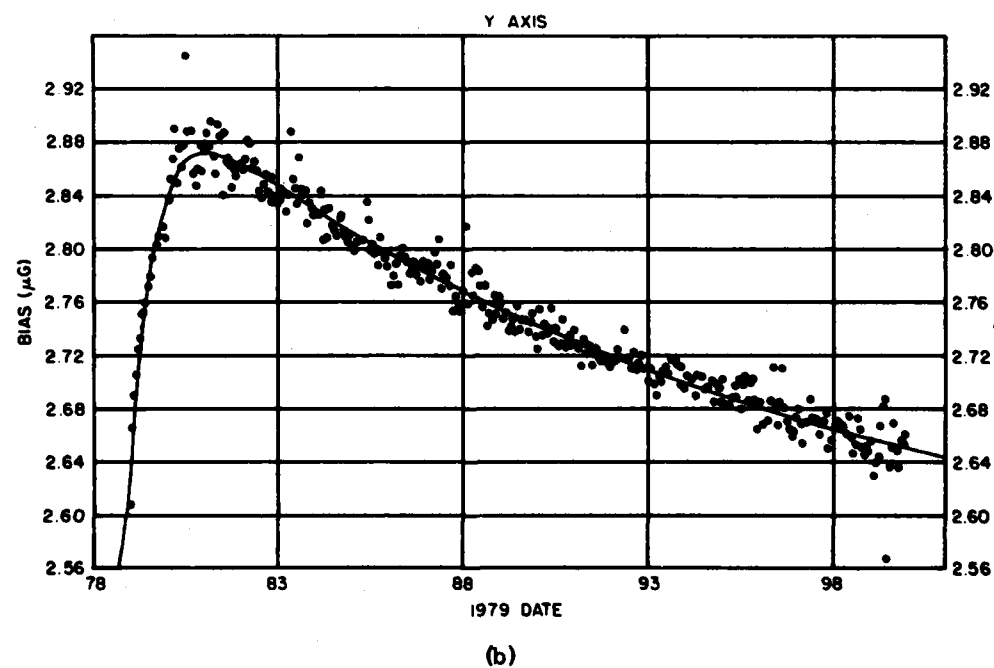
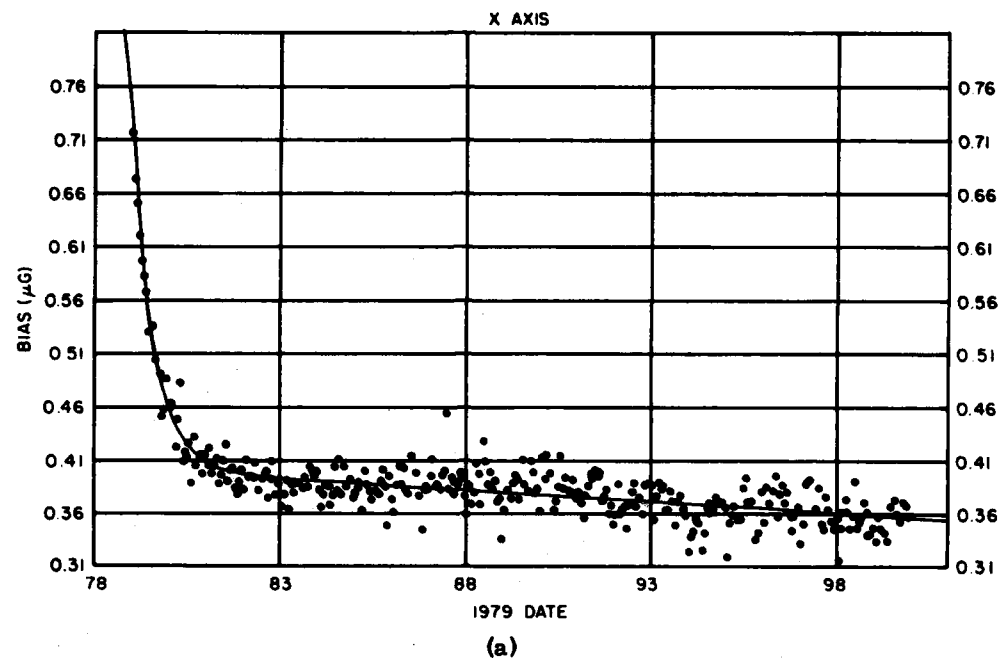


Figure 10. X-, Y-, and Z-axis Bias Values, Days 79079-79100

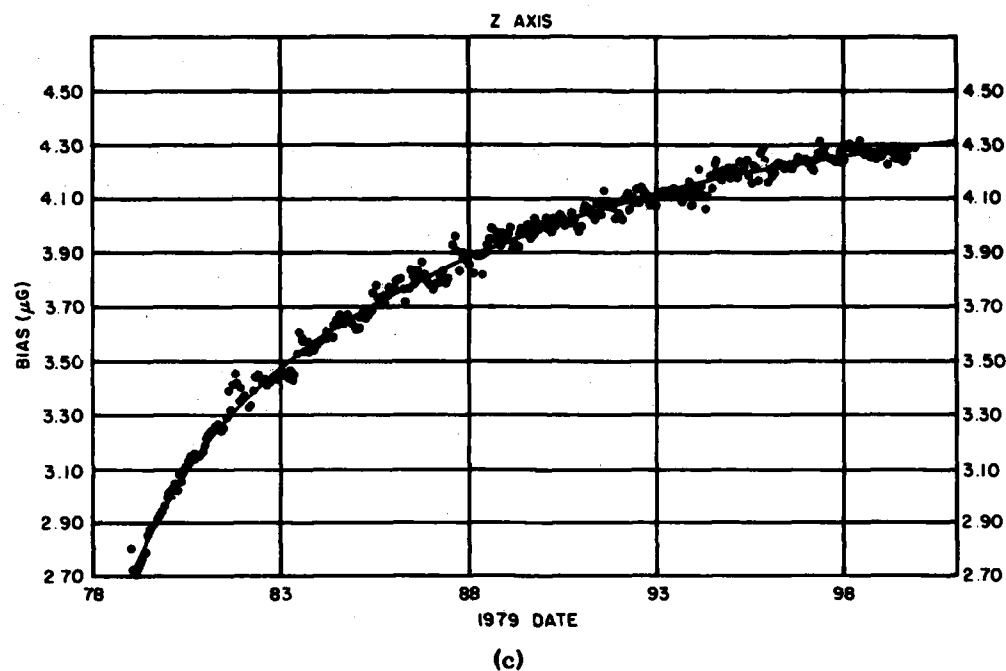


Figure 10. X-, Y-, and Z-axis Bias Values, Days 79079-79100 (Cont)

$$dC = \frac{1}{A_{ref}} \left\{ (\xi k + \gamma l + \eta t) \left[\gamma \cdot (1 + \operatorname{erf} \gamma S) + \frac{1}{S\sqrt{\pi}} e^{-\gamma^2 S^2} \right] \right. \\ \left. \left[+ \frac{l}{2S^2} (1 + \operatorname{erf} \gamma S) + \frac{1}{2} \sqrt{\frac{T_F}{T_1}} \left[\frac{\gamma\sqrt{\pi}}{S} (1 + \operatorname{erf} \gamma S) + \frac{1}{S^2} e^{-\gamma^2 S^2} \right] \right] \right\} dA, \quad (5)$$

where

$$dC = \frac{2 dF}{A_{ref} \rho V^2}$$

F = aerodynamic force

ξ, γ, η = direction cosines between mass velocity vector and axes of element of area, respectively

k, l, t = direction cosines between the axes of element of area, and the direction in which force is desired (accelerometer axis)

$\operatorname{erf} \gamma S$ = error function of γS

S = molecular speed ratio = (mass velocity of gas)/(most probable random speed of molecules)

T_i = temperature of incident molecules

T_r = temperature of reflected molecules (assumed = 300°K)

Eq. (5) is integrated over the entire satellite surface area to obtain the drag coefficient for a particular axis. Values appropriate to this satellite were used with Eq. (5) to derive drag coefficients.⁸ Figure 11 shows an example of drag coefficients for each axis as a function of pitch angle. These results were obtained by assuming a temperature (T_i) of 1000°K and a total satellite velocity of 8 km/sec along the Z axis. The values have been normalized by the satellite Z-axis cross-sectional area. Negative values indicate that the drag force is along the direction defined as negative for that axis.

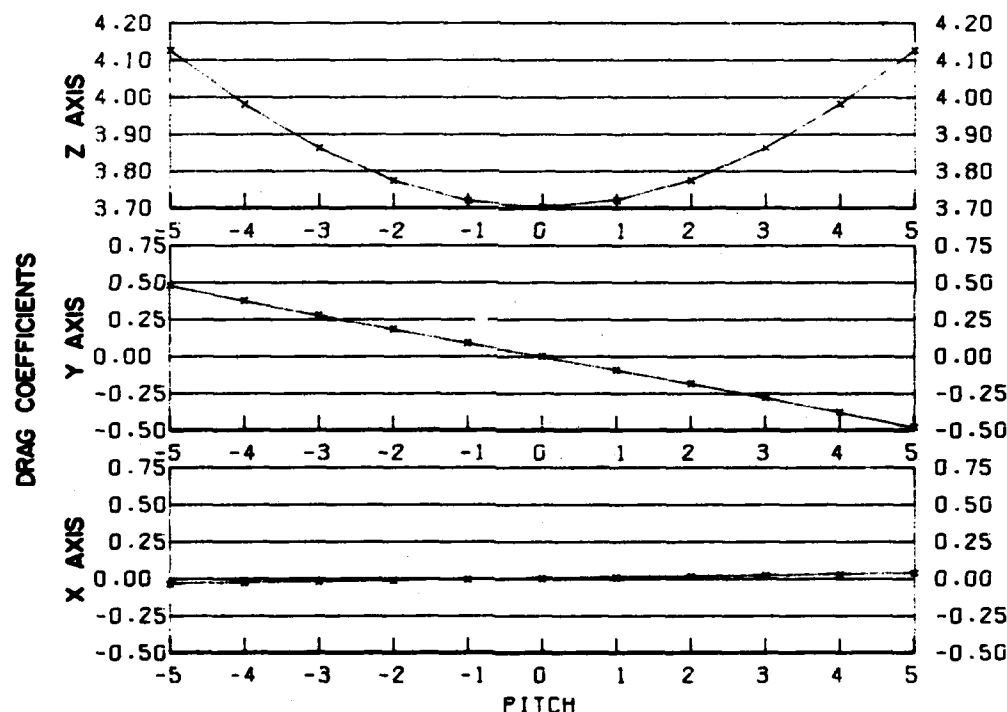


Figure 11. Drag Coefficients for X, Y, and Z Directions

In the solution of Eq. (3), only three acceleration measurements are available (a_i) while there are four unknowns (ρ , \vec{V}). An iterative technique has been developed to determine density and winds. The Z-axis satellite velocity (~ 8 km/sec) is

8. Mazzella, A.J., Jr., (1982) Drag Coefficients for a Satellite, AFGL Technical Report (in press).

large compared to its uncertainty, hence an initial estimate of the density is obtained by assuming $\vec{V}_0 = -\vec{V}_G + \vec{V}_A$ and calculating

$$\rho_0 = \frac{a_{DZ}}{\left(\frac{1}{2} \frac{A_{ref}}{m}\right) V_0^2 C_Z(V_0)} \quad (6)$$

This density is used to calculate the three velocity components, \vec{V} , and to obtain the wind as $\vec{V}_W = \vec{V} - \vec{V}_0$. To refine the solution a new $V = (V_X, V_Y, V_{0Z})$ is used to calculate a new ρ . This new ρ is then used to calculate new velocities. The process is repeated until the value of $|\vec{V}_{WZ}|$ is less than $0.02 |V_Z|$.

The errors in the calculated values of density are attributed to accelerometer bias, attitude uncertainties, drag coefficient estimates, noise within the desired signal frequency spectrum, and the inseparability of density and winds along the in-track axis. Systematic errors due to the drag coefficient are estimated to be within ± 5 percent, while those due to bias vary from ± 0.4 percent at 170 km to ± 2 percent at 220 km. Low frequency noise ($0.04 \mu g$) contributes a random error of ± 0.5 percent at 170 km and ± 2.5 percent at 220 km. In addition an assumed wind uncertainty of 200 m/sec along the Z axis contributes a random error of ± 5 percent. Attitude errors are negligible. For applications of the data requiring only knowledge of the drag, rather than the density, the errors are further reduced. The errors due to drag coefficient and Z-axis winds are eliminated. Further, if long-term average drag (order of one orbit) is required the low frequency noise average will be approximately zero. The major error contribution to cross-axis wind determination is the low frequency noise. The amplitude of this noise is $0.08 \mu g$ while the maximum acceleration due to wind is less than $0.1 \mu g$. As a result, there is a random error of ± 60 m/sec at 170 km and ± 160 m/sec at 200 km. Uncertainties in attitude and the Z-axis wind result in an additional random error of about ± 10 m/sec at all altitudes. By combining results from n orbits obtained during similar solar and geophysical conditions an average wind behavior can be derived with the error reduced by a factor of $n^{-1/2}$. A complete summary of the density and wind error analysis has been given elsewhere.⁹

5. GEOPHYSICAL STUDIES

Global studies of present and future SETA density and wind data will lead to an improved understanding of atmospheric dynamics and consequently to more accurate models. Upper atmosphere heating above 150 km is mainly by:

9. Mazzella, A. J., Jr. (1982) Error Analysis for Densities and Winds, AFGL Technical Report (in press).

- (1) solar electromagnetic energy at extreme ultraviolet wavelengths,
- (2) energy from the solar wind plasma resulting in particle heating and convection electric fields (Joule heating), and
- (3) upward propagating gravity waves and tides.

Gravity waves and winds are involved in transporting energy from the auroral zone to lower latitudes. The SETA data permit investigation of aspects of each of these effects. Section 5.1 gives a brief overview of these heat sources and describes how the satellite orbital characteristics relate to their study. Sample measurements from the operational SETA flight are applied to problems involving each heat source in turn in Section 5.2. Section 5.3 demonstrates the capability of the accelerometer to measure neutral winds. Although treated separately here, simultaneous wind and density data obtained on an every orbit basis over a wide latitude region for the first time, will be utilized in planned geophysical studies.

5.1 Relation of Data to Atmospheric Studies

5.1.1 NEUTRAL ATMOSPHERIC HEATING AND DYNAMICS OVERVIEW

The main source of thermospheric heating is the solar electromagnetic energy. It has major variations related to the eleven-year solar cycle and the twenty-seven day solar rotation period. This energy is deposited mainly at low latitudes and in the summer hemisphere. The density maximizes in the vicinity of the sub-solar point and reaches a minimum value near the anti-solar point. This diurnal variation is modulated by the seasonal migration of the sun's declination. Jacchia⁶ contains an excellent description of these variations. This density structure produces pressure gradients that cause an atmospheric circulation. An early wind model based on pressure gradients was developed by Kohl and King.¹⁰ A wind flow is set up essentially from the dayside to the nightside of the earth. Near the equator the winds are mainly zonal (eastward for local times later than the time of the diurnal maximum, westward for earlier local times). At higher latitudes the wind is predominately toward the pole on the dayside and away from the pole on the nightside. Typical wind speeds associated with the solar EUV heat source are of the order of 100 m/sec.

The solar wind, in contrast to the solar EUV, provides a heat source that is effective at high latitudes. The earth's approximately dipole magnetic field is radically modified beyond a few earth radii through interaction with the solar wind plasma that flows by earth with a velocity in excess of 400 km/sec. The effect of this supersonic flow on earth's geomagnetic field is to compress it on the dayside

10. Kohl, H., and King, J.W. (1967) Atmospheric winds between 100 and 700 km and their effects on the ionosphere, J. Atmos. Terr. Phys. 29:1045.

and elongate it (beyond the moon's orbit) on the nightside. This deflection of the magnetic field creates a cavity to which the solar wind does not have direct access. This cavity and its boundary regions are known as earth's magnetosphere. A schematic view of the magnetosphere is shown in Figure 12.¹¹ Its interior consists of several regions containing plasma with a variety of particle densities and energies. Electrodynamical coupling, or interaction, occurs between the magnetosphere, ionosphere, and upper atmosphere.¹² The mechanisms are not well understood. It is known that the magnetosphere affects the neutral upper atmosphere mainly by driving large-scale currents through the ionosphere. These currents result in Joule heating¹³ at auroral zone latitudes. Both the magnitude and spatial extent of the high latitude heating correlate with geomagnetic activity and are extremely variable. As a result, large and sudden density variations occur. Solar wind related energy is also deposited directly by particle precipitation. One mechanism involves electrons that are accelerated in the geomagnetic tail and precipitate at high latitudes. The polar "cusp" region (top of Figure 12) provides another means of particle precipitation. The cusp appears to be like a hole in the magnetosphere, permitting solar wind particles to directly enter the upper atmosphere. The affected region corresponds roughly to the noontime auroral oval.

Strong wind systems can be induced by the high latitude heating mechanisms. The circulation is driven from high latitudes to low latitudes. Its strength depends on the magnitude of the heat source. During large storms this circulation can reverse that due to solar EUV heating (for example, Straus et al,¹⁴ Straus,¹⁵ Dickinson et al¹⁶). These winds are a major mechanism for heat transport.

Atmospheric tides are regular large-scale oscillations excited by gravitational forces of the sun and moon or by absorption of solar radiation. They have a basic period of one lunar or one solar day with higher harmonics down to a period of six lunar or solar hours. Previous accelerometer data have shown that below 200 km the amplitude of the solar semidiurnal variation exceeds that of the diurnal

11. Stern, D. P. (1978) Solar Terrestrial Programs: A Five Year Plan, NASA Goddard Space Flight Center, Greenbelt, Maryland.
12. Stern, D. P. (1977) Large-scale electric fields in the earth's magnetosphere, Rev. Geophys. Space Phys. 15:156.
13. Cole, K. D. (1962) Joule heating of the upper atmosphere, Aust. J. Phys. 15:223.
14. Straus, J. M., Creekmore, S. P., Harris, R. M., and Ching, B. K. (1975) Effects of heating at high latitudes on global thermospheric dynamics, J. Atmos. Terr. Phys. 37:1545.
15. Straus, J. M. (1978) Dynamics of the thermosphere at high latitudes, Rev. Geophys. Space Phys. 16:183.
16. Dickinson, R. E., Ridley, E. C., and Roble, R. G. (1981) A three-dimensional general circulation model of the thermosphere, J. Geophys. Res. 86:1499.

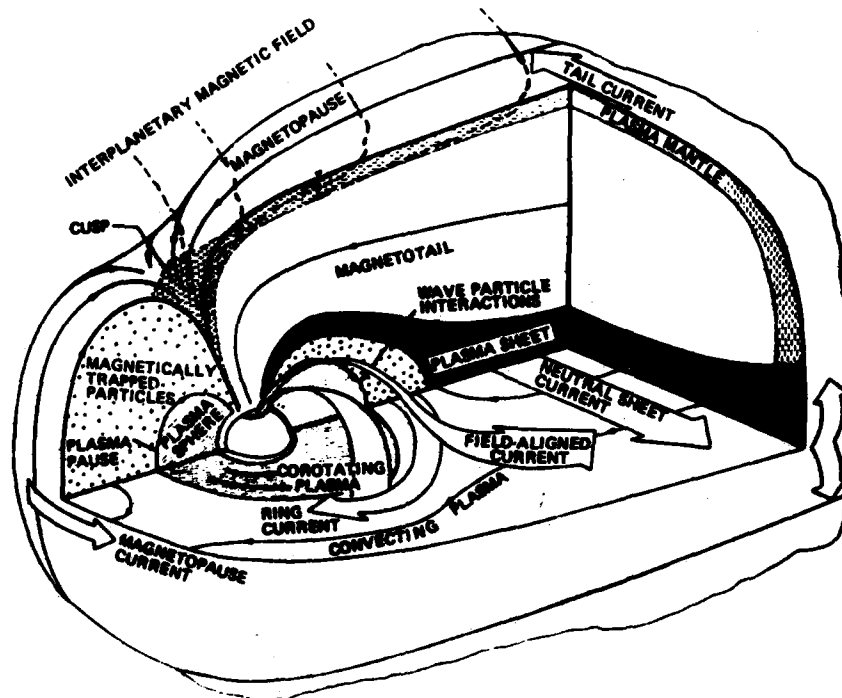


Figure 12. Diagram of Earth's Magnetosphere

bulge^{1, 17} and that the phase of the diurnal variation shifts to later local times from the equator to mid-latitudes.¹⁸ Tidal phenomena have been reviewed recently by Forbes and Garrett.¹⁹

Large-scale gravity waves, having periods different from those of tidal waves and not directly related to the earth-moon-sun geometry, also occur in the atmosphere. These waves may be generated either locally in the thermosphere or near the earth's surface. Those originating in the thermosphere are frequently associated with the energy released in a narrow zone at auroral latitudes during geomagnetic storms. Theoretical studies have shown that the atmosphere acts as a filter, allowing only longer wavelengths (hundreds of km) to propagate a significant distance from the auroral zone.^{20, 21} Waves propagating into the thermosphere from below have been postulated to result from earth's orographic features, weather fronts, and jet stream turbulence. Evidence of a tropospheric source for wavelike features in density profiles has been presented by Rice and Sharp.²²

The numerous heating and circulation processes involved in determining atmospheric variability are summarized in Figure 13.²³ (This figure also includes

Because of the large number of references cited above, they will not be listed here. See References, pages 51 and 52.

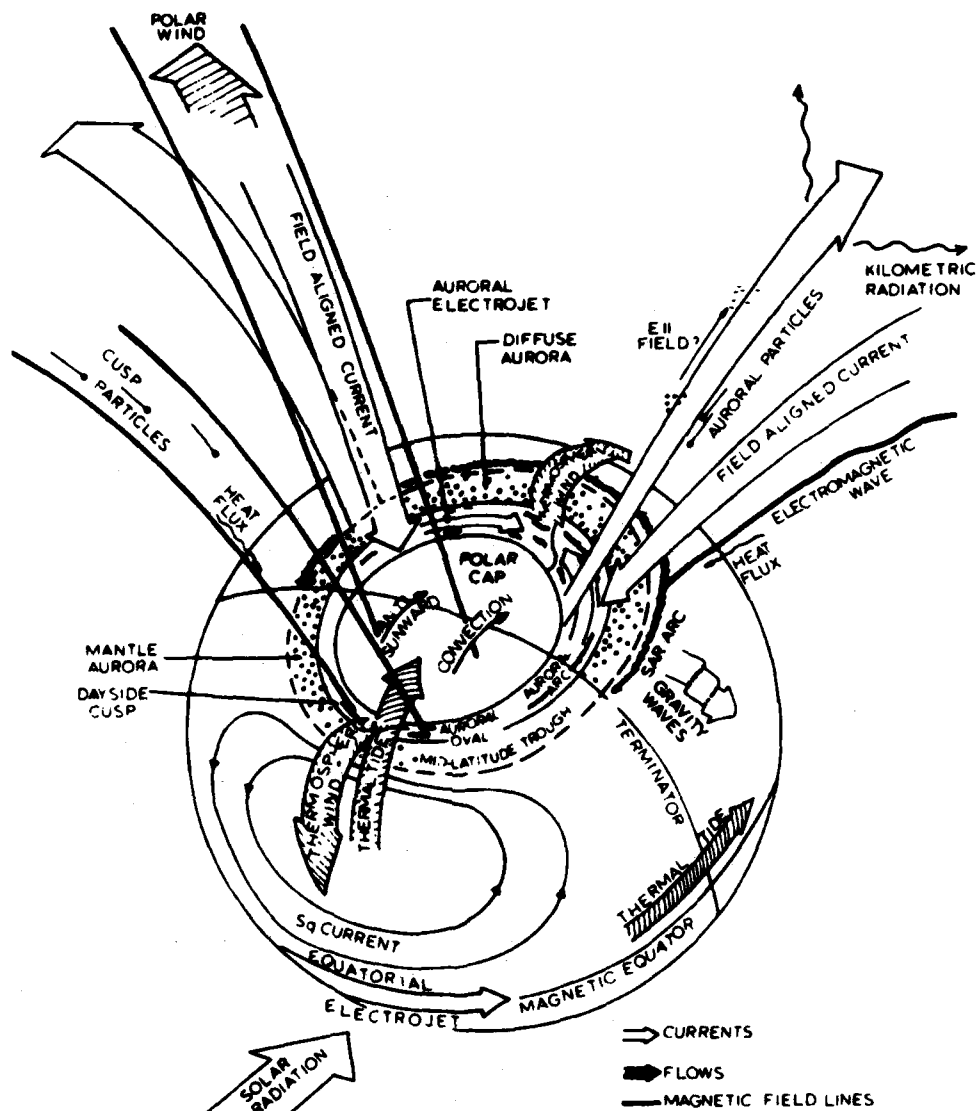


Figure 13. Heat Sources for the Upper Atmosphere

processes outside the scope of the present discussion). Both neutral and ionized constituents exhibit regular global patterns as well as significant short-term variations. During geomagnetically quiet times the thermosphere is driven mainly by solar electromagnetic energy. High latitude processes dominate during large geomagnetic storms. At other levels of geomagnetic activity an intermediate condition prevails. To develop more accurate models our knowledge of the magnitude and distribution of atmospheric heating must be improved considerably.

5.1.2 ORBITAL DATA COLLECTION

The normal data collection mode for the accelerometer is continuous operation in the most sensitive (C) range. This permits drag acceleration measurements to be obtained over a complete orbit on every orbit. High accuracy density data are obtained over about a 150° -latitude band, and winds are obtained over about a 100° -latitude band with an accuracy of the data that is a function of satellite altitude, as discussed in Section 4. Figure 14 summarizes the orbital characteristics with respect to the northern hemisphere auroral zone for a one day period. Geomagnetic latitude and magnetic local time coordinates are used, and are indicated on

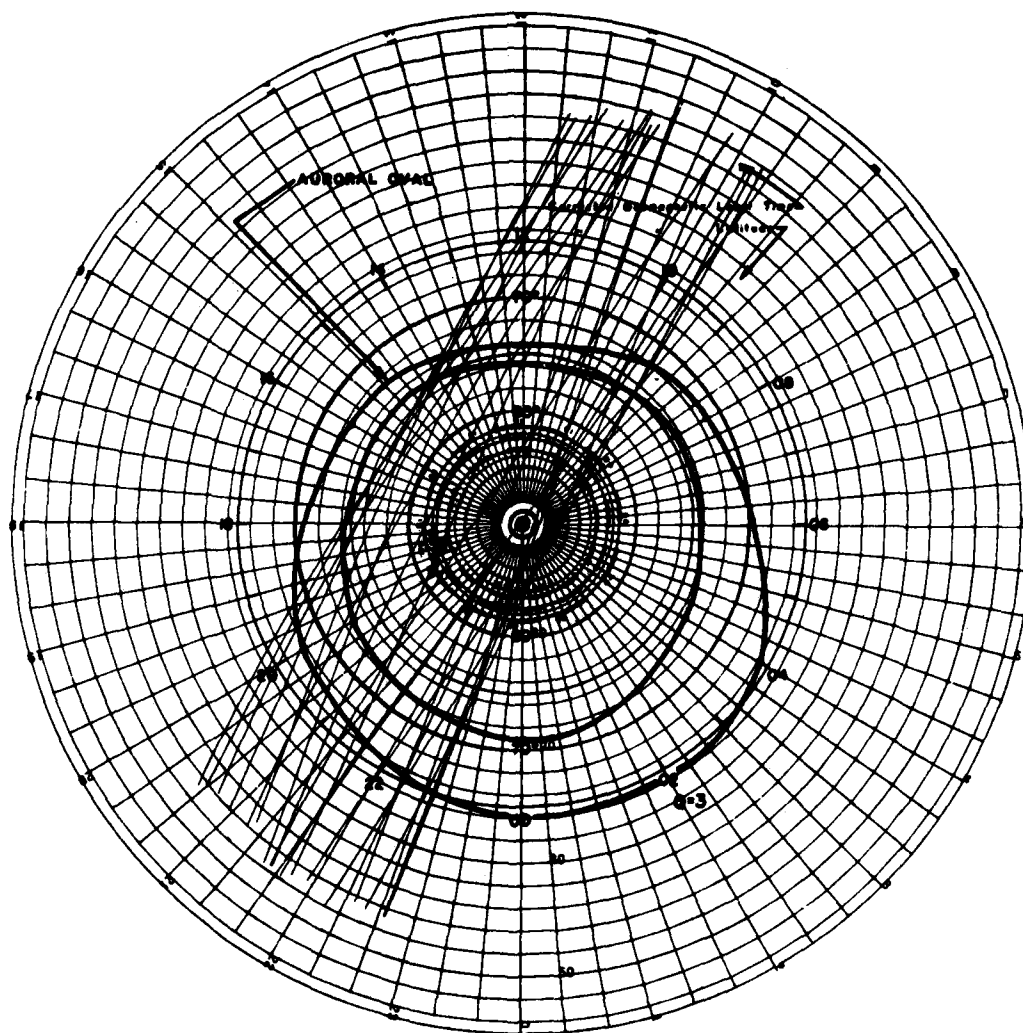


Figure 14. Intersection of Satellite Tracks for One Day With Northern Hemisphere Auroral Zone

the figure. This permits plotting the satellite track with respect to a fixed auroral zone. Because of the high satellite inclination and relatively low eccentricity, both the day and night auroral regions are sampled on every orbit at approximately the same altitude.

The combination of continuous operation for an extended period of time over a wide latitude region with routine high temporal resolution auroral zone data has not been achieved with previous accelerometer flights. These factors provide a unique opportunity to investigate the role of the various heat sources on the neutral atmosphere.

5.2 Atmospheric Density Results

An example of an atmospheric density profile is shown in Figure 15. Density (g cm^{-3}) is plotted as a function of the following parameters: GMT (seconds), geographic latitude, geomagnetic latitude, local time (hours and minutes), GMT (hours and minutes), and altitude (km). These results were obtained during the geomagnetic storm to be discussed in Section 5.2.2. Superimposed on the general increase of density with decreasing altitude are significant oscillations. These wave structures are described further in Section 5.2.3.

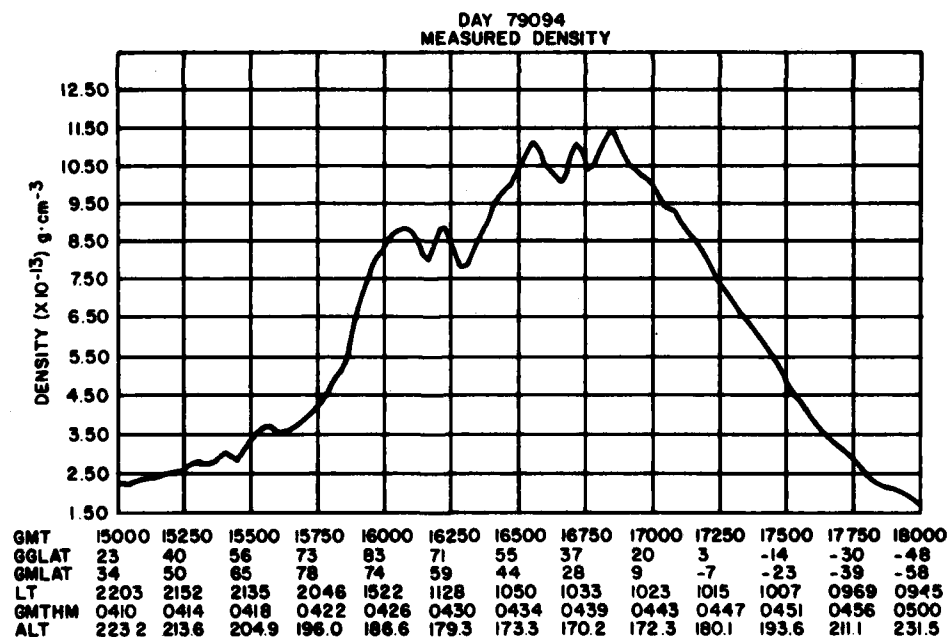


Figure 15. Atmospheric Density as a Function of Altitude, Latitude, and Local Time

5.2.1 SOLAR FLUX EFFECTS

Thermospheric heating by solar EUV radiation is represented by a strong positive correlation of density and the solar radio flux measured at 10.7 cm ($F_{10.7}$) in all current atmospheric models. The radio flux is assumed to track variations in EUV flux and thus reflect variations in the thermospheric energy input. The long-term component (primarily related to the 11-year solar cycle) is represented by a flux averaged over several (usually three) solar rotation periods (\bar{F}). The short-term component related to daily changes in solar activity is represented by $(F - \bar{F})$ where F has a lag of about one day. An empirical relationship between density and solar flux has been derived for low solar flux conditions ($\bar{F}_{10.7} \leq 100$) by Marcos and Champion²⁴ using regression techniques described in Marcos et al.²⁵ An extension to high solar flux conditions based on measured data is required since a linear extrapolation may not be an accurate representation.

Figure 16 shows the trend of the density variability at 200 km with solar flux as determined from accelerometer data. The solid line represents the relation derived for $\bar{F}_{10.7} \leq 100$ from Marcos and Champion.²⁴ The dashed line is a linear extrapolation of this result. Circles represent data obtained during several days in April 1978, a period of moderate solar activity, with the ROCA experiment on the S3-4 satellite.²⁶ Data were obtained over a five-month period, but due to processing problems at SAMTEC, delivery of data tapes to AFGL were considerably delayed. Routine processing of the data commenced during CY 1981. SETA data for several days in April 1979, a period of high solar flux, are shown as crosses. For comparison, values predicted by the MSIS model²⁷ are shown as triangles. The accelerometer data indicate a larger response to solar flux than the MSIS model. A quantitative empirical estimate of the density increase per unit solar flux increase will be derived with additional ROCA and SETA data. The result can be directly utilized to extend the present empirical model.

24. Marcos, F.A., and Champion, K.S.W. (1979) Empirical model of lower thermospheric density for low solar flux and quiet geomagnetic conditions, Space. Res. 19:89.
25. Marcos, F.A., Garrett, H.B., Champion, K.S.W., and Forbes, J.M. (1977) Density variations in the lower thermosphere from analysis of the AE-C accelerometer measurements, Planet. Space Sci. 25:499.
26. Marcos, F.A., and Champion, K.S.W. (1979) Satellite Density Measurements with a Rotatable Calibration Accelerometer (ROCA), AFGL-TR-79-0005, ADA 069740.
27. Hedin, A.E., Salah, J.E., Evans, J.V., Reber, C.A., Newton, G.P., Spencer, N.W., Kayser, D.C., Alcayde, D., Bauer, P., Cogger, L., and McClure, J.P. (1977) A global thermospheric model based on mass spectrometer and incoherent scatter data, MSIS 1, N₂ density and temperature, J. Geophys. Res. 82:2139.

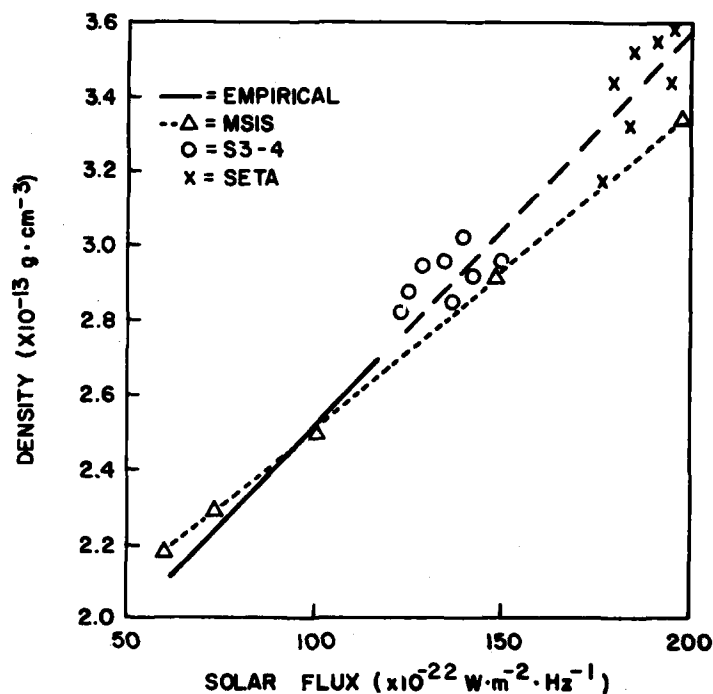


Figure 16. Atmospheric Density as a Function of Solar Flux

5.2.2 GEOMAGNETIC ACTIVITY EFFECTS

Rapid global fluctuation of atmospheric density with a typical duration of one to several days are connected with the solar wind related geomagnetic disturbances. The amplitude of the density increase generally depends on the strength of the geomagnetic storm as measured by the three-hourly planetary index K_p . The atmospheric response occurs first at auroral zone latitudes and then at low latitudes with a delay of about 6 to 8 h. This implies that the energy transferred to the thermosphere through auroral processes at high latitudes is later distributed globally through dynamic processes.²⁸ Recent composition measurements and theoretical studies have shown that atmospheric winds driven by the high latitude heat source produced by the magnetic storm are involved in the global redistribution of energy and mass.²⁹ The phase and amplitude of the atmospheric response as a function

28. Forbes, J.M., Marcos, F.A., and Champion, K.S.W. (1978) Lower thermosphere response to geomagnetic activity, *Space Res.* 13:173.

29. Mayr, H.G., and Hedin, A.E. (1977) Significance of large-scale circulation in magnetic storm characteristics with applications to AE-C neutral composition data, *J. Geophys. Res.* 82:1227.

of latitude are not well modelled at present. The effect also varies with longitude, season, local time, and solar flux.

Figure 17a shows the response of the atmosphere to a large geomagnetic disturbance. Density measured at 80° , 60° , 30° , and 0° north geographic latitude at about 1030 h LT and Kp are plotted as a function of time for the period 1200 h, day 79093 to 2400 h, day 79094 GMT. The curves therefore show density values obtained on the dayside of the atmosphere during 24 consecutive orbits. The altitude at a given latitude varies slightly during this period due to perigee precession. The densities at each latitude have been normalized to a constant altitude, indicated for each curve.

An increase in Kp starts at 1500 h on day 93 and rises to a maximum value of 8 for the three-hour interval beginning at 2100 h. A density increase occurs at 80° and 60° in response to the first Kp increase, but not at the lower latitudes. In addition to this phase difference, another feature is the greater intensity of the thermospheric response at high latitudes. At lower latitudes the density continues to increase while Kp decreases. A mechanism for maintaining these enhanced densities is the large-scale circulation pattern with rising motions at high latitudes and descending motions at middle and low latitudes described by Mayr et al.³⁰

Figure 17b shows the atmospheric response predicted by the Jacchia 1977³¹ model that utilizes a latitude-dependent time delay for the geomagnetic activity effect. Model values at the same latitudes and altitudes as Figure 17a are given. At each latitude the amplitude and phase of the model densities follow the Kp variation with a time delay. This is in contrast to the complex density structure actually measured at high latitudes and the gradual density increase found at lower latitudes. Hence the model gives a poor representation of the atmospheric density response to this geomagnetic storm. A comprehensive analysis of geomagnetic activity variations detected with SETA data has been initiated. An improved description of this phenomenon is an important requirement for improved atmospheric models.

5.2.3 WAVE STRUCTURES

Gravity waves with largest amplitudes observed at high latitudes were detected by the accelerometers on the OV 1-15 satellite.³² These were related to the

30. Mayr, H.G., Harris, I., and Spencer, N.W. (1978) Some properties of upper atmosphere dynamics, Rev. Geophys. Space Phys. 16:539.

31. Jacchia, L.G. (1977) Thermospheric Temperature, Density and Composition: New Models, Spec. Rep. 375, Smithsonian Astrophys. Observ., Cambridge, Mass.

32. Marcos, F.A., and Champion, K.S.W. (1972) Gravity waves observed in high latitude neutral density profiles, Space Res. 12:76

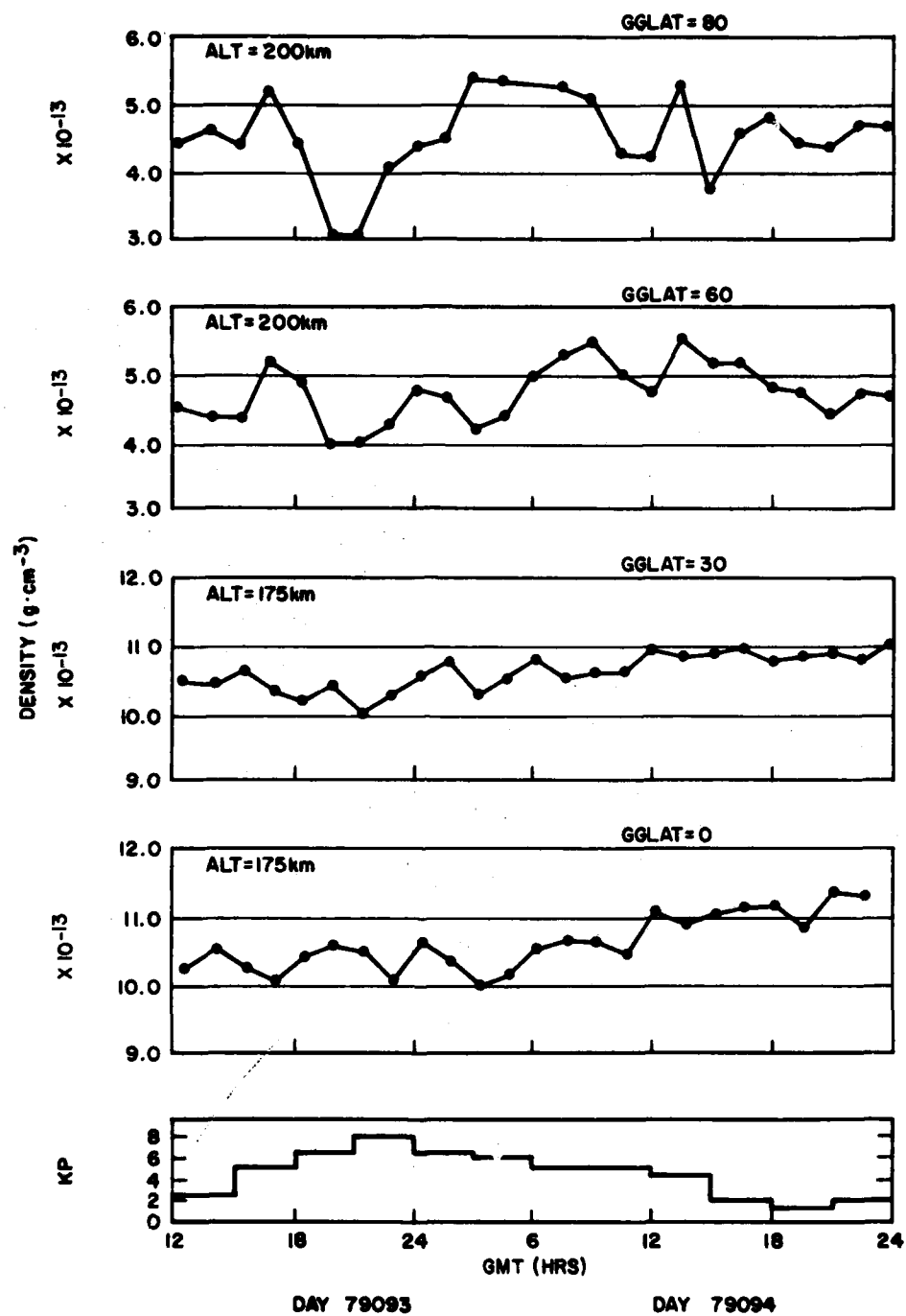


Figure 17a. Atmospheric Density Response to a Geomagnetic Storm

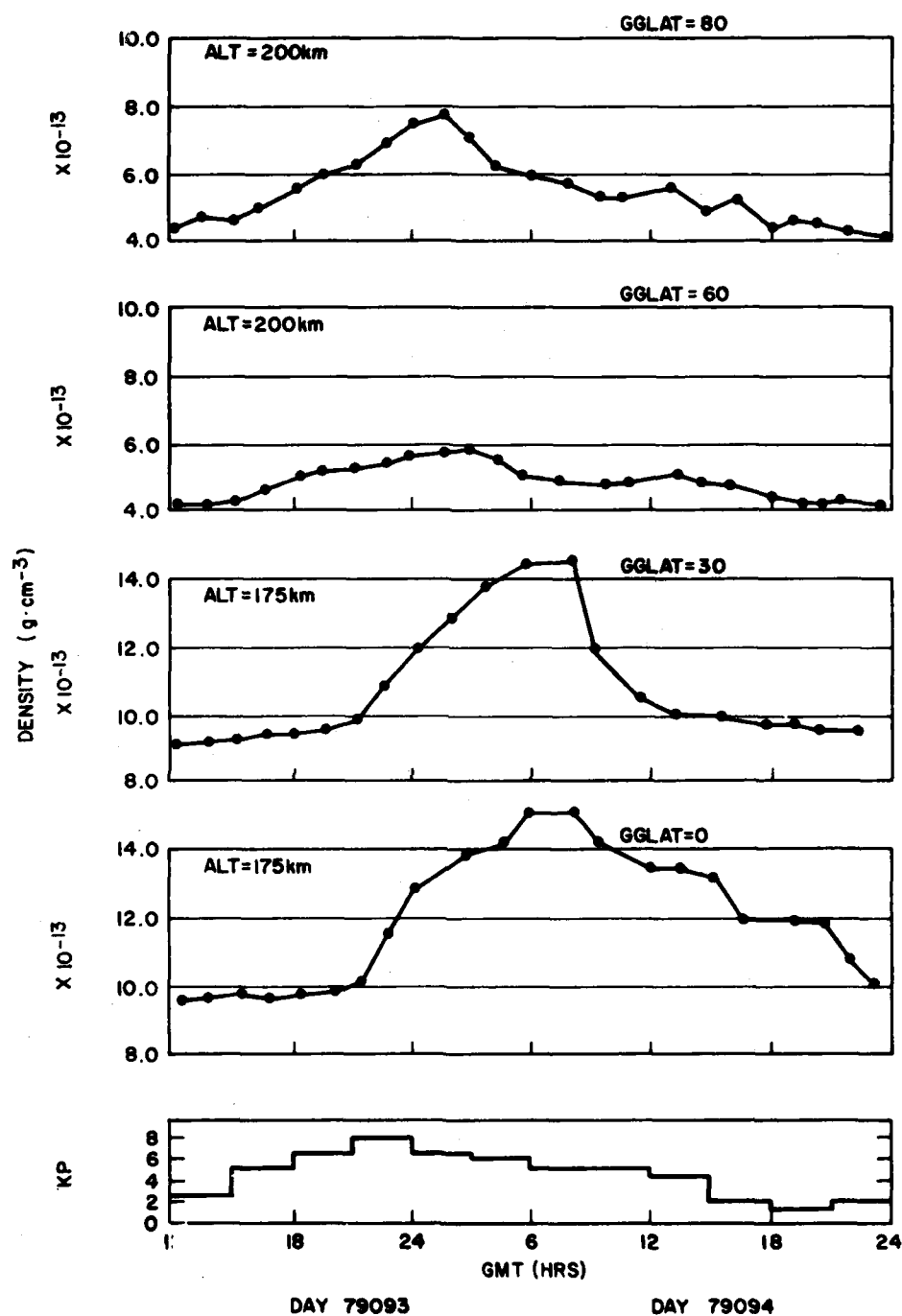


Figure 17b. Model Prediction of Density Response to a Geomagnetic Storm

intensity of heating as indicated by the auroral electrojet (AE) index by Forbes and Marcos.³³ Theoretical models describing the spectrum of waves generated by high latitude heating show occurrence of long wavelengths of the order of 3000 km.²⁰ Evidence of wave structures with location dependent on earth's tropospheric weather patterns have been found in Atmosphere Explorer satellite data by Rice and Sharp.²² SETA results provide a unique opportunity to statistically distinguish between waves originating in the lower and upper atmosphere. Their respective characteristics can be studied over a wide latitude region on an every-orbit basis.

Figure 18 shows the nature of wavelike disturbances associated with geomagnetic activity. Density data obtained during one orbit of the storm period discussed in the previous section are plotted as a function of time and latitude. To indicate better the wave structure features, the exponential dependence of density with altitude has been removed by normalizing the data to an altitude of 200 km. This facilitates detection of the wave half-amplitude, determined as the deviation from a smooth curve obtained through the density data. The largest half-amplitudes of about -22 percent and +27 percent occur at 15625 sec GMT and 16050 sec GMT respectively. In geomagnetic coordinates these maxima both correspond to about 72°N on the nightside and dayside respectively. The data clearly show a decrease in the amplitude of the oscillatory behavior with latitude away from the auroral zone. The apparent horizontal wavelengths are estimated by the time between successive density maxima or minima multiplied by the satellite velocity. Values of the order of 1500 to 4000 km are observed. It is concluded that these results are consistent with gravity waves generated by auroral sources during a period of high geomagnetic activity. This sample of data demonstrates the capability of the accelerometer to provide knowledge of the detailed structural atmospheric features. These measurements are required for a more comprehensive understanding of atmospheric perturbations.

5.3 Neutral Atmospheric Wind Results

The importance of neutral winds in determining the global density structure was indicated in Section 5.1. There have been few satellite measurements of neutral winds. A review of several techniques and their limitations has been given by Hanson and Heelis.³⁴ Samples of wind data were obtained from experiments on the AE-C satellite. Results reported to date have been extremely limited. The

33. Forbes, J.M., and Marcos, F.A. (1973) Thermospheric density variations associated with auroral electrojet activity, *J. Geophys. Res.* 78:3841.

34. Hanson, W.B., and Heelis, R.A. (1975) Techniques for measuring bulk gas motions from satellites, *Space Sci. Instrum.* 1:493.

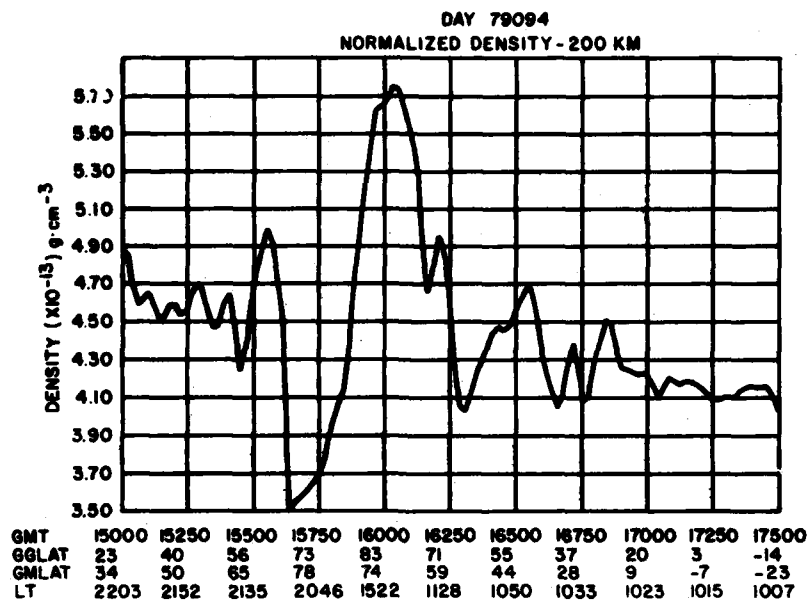


Figure 18. Wave Structure in an Atmospheric Density Profile

Neutral Atmosphere Temperature Experiment³⁵ has detected vertical winds.³⁶ A technique for obtaining along-track winds with the Open Source Spectrometer³⁷ was described by Knutson et al.³⁸ Cross-axis winds from the MESA accelerometer² have been derived for several orbits by Hanson et al.³⁹ Accelerometer horizontal wind measurements were also obtained during part of the four day flight of the LOGACS experiment.^{40, 41} The SETA accelerometer has demonstrated a capability

35. Spencer, N.W., Niemann, H.B., and Carignan, G.R. (1973) The neutral-atmosphere temperature instrument, Radio Sci. 8:284.
36. Spencer, N.W., Theis, R.F., Wharton, L.E., and Carignan, G.R. (1976) Local vertical motions and kinetic temperature from AE-C as evidence for aurora-induced gravity waves, Geophys. Res. Lett. 3:313.
37. Nier, A.O., Potter, W.E., Hickman, D.R., and Maursberger, K. (1973) The open-source neutral mass spectrometer on Atmosphere Explorer-C, -D, and -E, Radio Sci. 8:271.
38. Knutson, J.R., Kayser, D.C., and Potter, W.E. (1977) Mass spectrometric measurement of thermospheric wind, J. Geophys. Res. 82:5253.
39. Hanson, W.B., Coley, N.R., and Heelis, R.A. (1980) Study of Upper Atmosphere Wind Motions, AFGL-TR-80-0307, ADA 097733.
40. Feess, W.A. (1973) Logacs Wind Analysis, USAF Rep. SAMSO-TR-73-355, Space and Missiles System Organization, Los Angeles, California.
41. Pearson, J.A. (1973) The Low-G Accelerometer Calibration System Orbital Accelerometer System, Rept. TR-0074(4260-10)-1, Aerospace Corp., Los Angeles, Calif.

to measure cross-axis winds over a wide latitude region. Analysis of these results will significantly enhance our understanding of global transport processes and consequently atmospheric density variability. The wind data are discussed separately in this section to emphasize their significance. However, these results will be most fully exploited by analyzing them in conjunction with the simultaneously measured density data.

Two wind profiles derived from cross-track data are given in this section. These horizontal winds were measured near the end and at the maximum, respectively, of the geomagnetic storm on day 79094. The major features of the observed winds are described. More comprehensive analyses will be provided in forthcoming reports. Vertical acceleration data obtained for the same time periods are also shown. At present, these have not been reduced to wind values. A detailed study of possible satellite motions in the radial direction is being made to ensure extraction of vertical atmospheric motions with high accuracy. Vertical wind results will also be the subject of a later report.

Because the orbit is not strictly polar, the angle between the zonal wind component and the accelerometer sensing axis is a function of geographic latitude. Figure 19 shows this relationship. As the pole is approached, the component of cross-axis wind measured shifts from mainly zonal toward meridional. Figure 20 shows filtered acceleration data from the X axis. A three-orbit period on day 79094, when Kp was moderately low, is presented to demonstrate the repeatability of these data. The rotation velocity, assumed to follow that of the earth, is about 460 m/sec at the equator and decreases with latitude to zero m/sec near the poles. (To derive the horizontal wind component the accelerations due to atmospheric rotation are removed as discussed in Section 4.) The aerodynamic side accelerations induced by this motion can be seen in each of the three orbits. The maximum (negative) acceleration caused by the eastward atmospheric motion occurs at mid-latitude near minimum altitude. At higher latitudes the amplitude of this modulation decreases. This is due to the slower rotation speed, the changing angle of attack and a lower density at the corresponding higher altitudes. As the satellite moves over the pole the winds due to atmospheric rotation are directed at its opposite side. As a result a positive acceleration output is sensed.

Neutral horizontal winds derived from the first orbit of the data of Figure 20 are shown in Figure 21. Velocity, in units of m/sec, is plotted as a function of GMT, geographic and geomagnetic latitude, local time, and altitude. Positive velocities indicate winds blowing from west-to-east on the dayside of the earth. On the nightside positive velocities indicate westward winds. At low and middle latitudes the daytime winds are observed to be mainly west-to-east with velocities of about 100 to 200 m/sec. If the diurnal bulge were located at 1600 h, the pressure gradients at low latitudes and a longitude corresponding to about 1030 h would drive

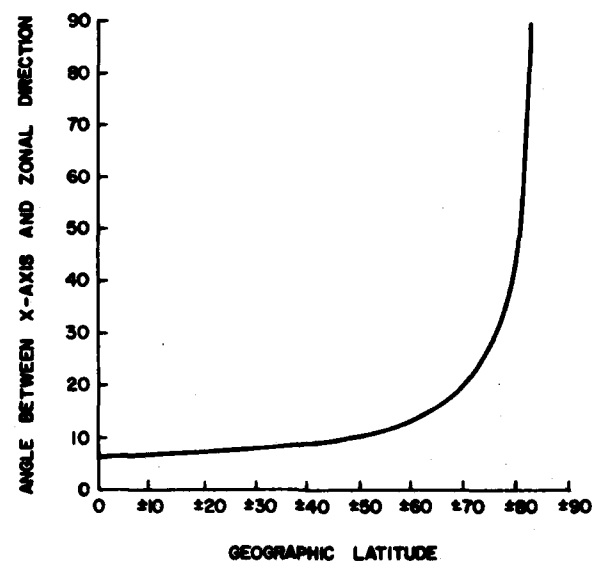


Figure 19. Accelerometer Cross-axis Angle of Attack vs Geographic Latitude

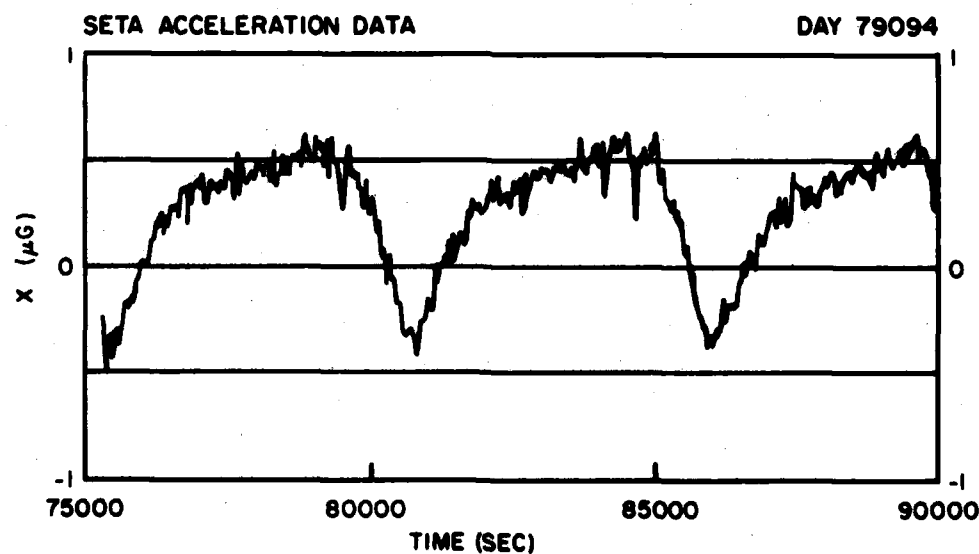


Figure 20. Cross-axis Acceleration Data During a Period of Moderately Low Geomagnetic Activity

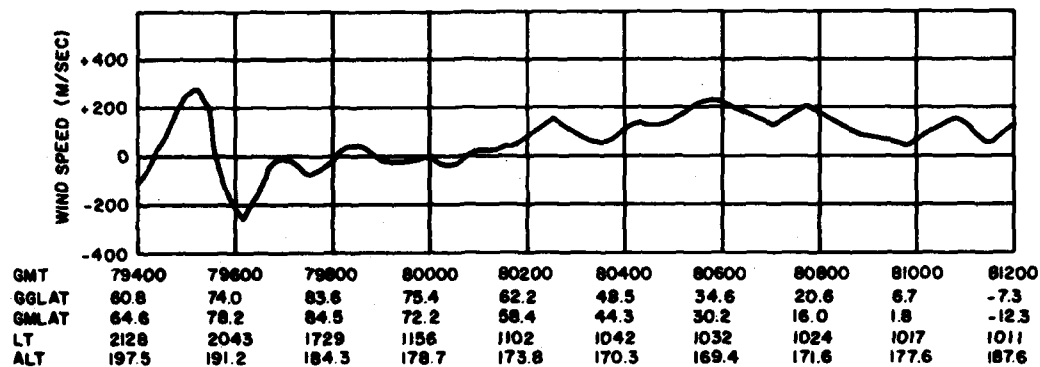


Figure 21. Horizontal Wind Velocities During a Period of Moderately Low Geomagnetic Activity

a wind in the opposite direction (east-to-west). Hence these observed winds are not consistent with a sub-solar density bulge. However, as noted in Section 5.1, the semidiurnal tide predominates below 200 km and is a possible mechanism for the observed wind direction. At higher latitudes from about 70 to 83° gg (geographic latitude) on the dayside, the winds are generally westward with speeds of 0 to 50 m/sec. On the nightside the winds are again generally west-to-east. However, these results are dominated by a shift to an east-to-west flow between 64.8° gg (68.8° gm) and 71.5° gg (75.6° gm) with a maximum velocity of 277 m/sec at 68.8° gg (72.9° gm). These large wind values may be an effect of the diminishing geomagnetic storm rather than a persistent feature. This will be resolved with the reduction of more data.

Figure 22 shows cross-axis acceleration data obtained earlier on day 79094 for a three-orbit period when the level of geomagnetic activity was high. Considerable structure is seen at high latitudes in contrast to the data of Figure 20. The wind profile derived for one orbit is shown in Figure 23. This orbit corresponds to a time when $K_p = 8$, the maximum value for this storm. Significant structure is observed at high latitudes. The maximum wind velocity for this orbit is 597 m/sec. It occurs on the nightside of the earth at 81.6° gg (78.0° gm). On the dayside there is a sharp transition with the winds shifting from westward to eastward at $<77.2^\circ$ gg (65.7° gm). This feature was also observed in the LOGACS data during extremely high geomagnetic conditions.^{42,43} The maximum eastward wind is 475 m/sec at 72.2° gg (60.7° gm). At latitudes below 60° N gg the wind is eastward at about

42. DeVries, L. L. (1972) Analysis and interpretation of density data from the low-G accelerometer calibration system (LOGACS), *Space Res.* 12:177.

43. Wu, S. T., Matsushita, S., and DeVries, L. L. (1974) An analysis of the upper atmospheric wind observed by Logacs, *Planet. Space Sci.* 22:1036.

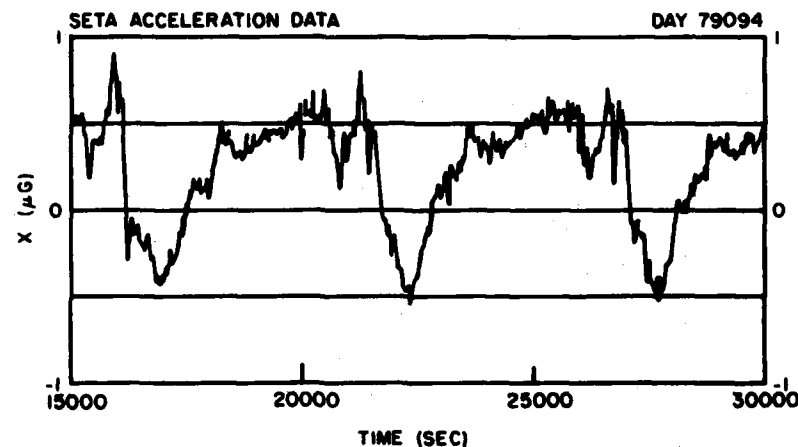


Figure 22. Cross-axis Acceleration Data During a Period of High Geomagnetic Activity

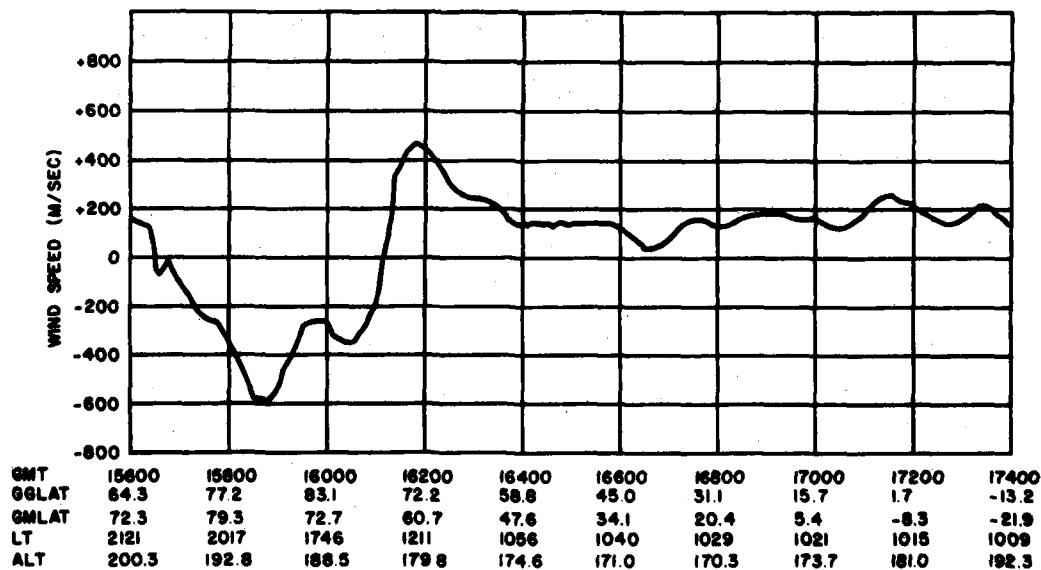


Figure 23. Horizontal Wind Velocities During a Period of High Geomagnetic Activity

100 to 200 m/sec, implying that the storm effects are confined to high latitudes. Hernandez and Roble⁴⁴ have suggested that a large-scale electric field associated with magnetospheric convection could explain an abrupt transition in zonal winds. The observed features appear to be related to large amounts of energy being deposited locally at high latitudes and being subsequently distributed globally. Pressure gradients associated with high latitude heating significantly modify the flow expected from solar EUV heating. The two examples of horizontal winds (Figures 21 and 23) demonstrate the complexity of the global wind field. Analysis of the full set of SETA measurements will permit resolution of many features of the flow of energy and momentum in the thermosphere.

Figure 24 shows radial axis filtered acceleration data. Figure 24a corresponds to the time period of Figure 20 and Figure 24b corresponds to the time period of Figure 22. Data for all six orbits show characteristic "bumps" occurring near perigee and near 50°S. These bumps correspond to an increased downward acceleration. If interpreted as vertical velocities, the accelerations of Figure 24 are of the order of 50 to 100 m/sec. Presently, vertical speeds of the order of a few m/sec have been predicted. There does not appear to be a significant dependence on geomagnetic activity. No attempt to interpret these results will be given here. The data are of extreme interest and will be thoroughly analyzed.

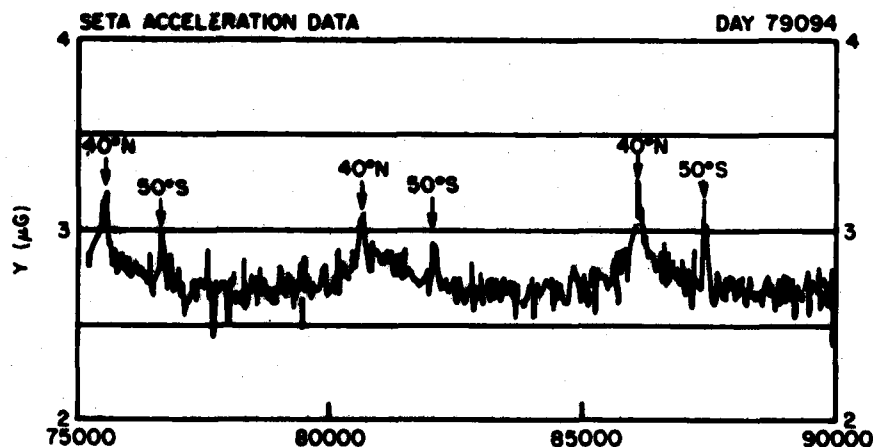


Figure 24a. Radial-axis Acceleration Data During a Period of Moderately Low Geomagnetic Activity

44. Hernandez, G., and Roble, R.G. (1976) Direct measurements of nighttime thermospheric winds and temperatures. 2. Geomagnetic storms. *J. Geophys. Res.* 82:5505-5511.

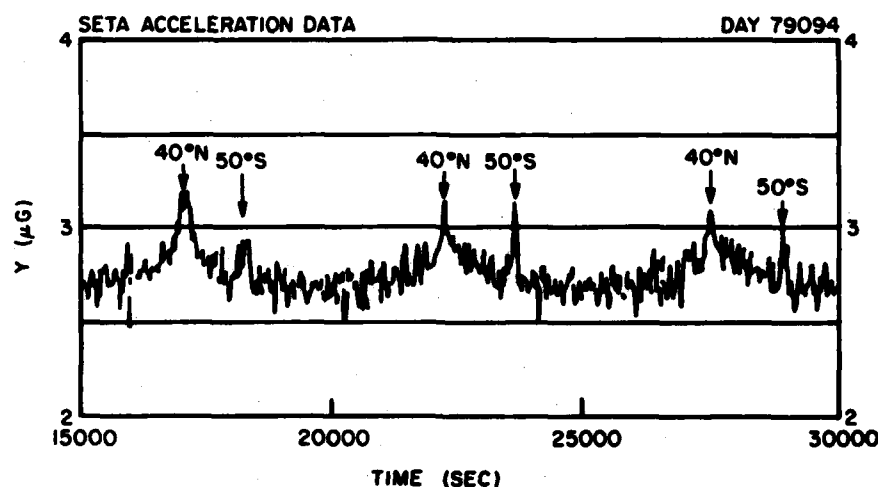


Figure 24b. Radial-axis Acceleration Data During a Period of High Geomagnetic Activity

6. CONCLUSIONS

An accelerometer has been developed using a single proof mass to measure simultaneously satellite accelerations in three orthogonal axes. The instrument is based on the design of the highly successful *single-axis MESA* accelerometer. Future instruments will be modified to eliminate bias drift anomalies.

Specific applications of the extremely accurate data obtained during a 22-day period of one flight demonstrated the importance of this data in solving geophysical problems. Density variations related to long-term (solar cycle) and short-term (geomagnetic activity and related wave propagation) phenomena were shown in Section 5 to provide valuable inputs to improve current empirical atmospheric models. A most significant development of this flight was the capability to detect wind motion for the first time over a wide latitude region on an every-orbit basis. Detailed knowledge of the spatial and temporal wind features permit extension of theories of atmospheric density dynamics and will provide fundamental knowledge of the magnetosphere-ionosphere-neutral atmosphere coupling. Maximum advantage of the data will be taken by performing studies of the simultaneous features of density variability, the occurrence of wave structure and the neutral wind motions. Where possible, other data, such as incoherent scatter (for example, Evans⁴⁵) measurements of temperature and plasma motions will be incorporated into coordinated analyses.

45. Evans, J. V. (1975) A review of F region dynamics, Rev. Geophys. Space Phys. 13:887.

Studies of data from the SETA flight will be extended to examine numerous other atmospheric structure features. These include horizontal wind and neutral density variations as a function of latitude, longitude, and local time. Data obtained in the high latitude regions will be of particular importance for elucidation of heating characteristics. The accuracy with which vertical winds can be extracted will also be determined. Their measurements would provide significant new information regarding the circulation of the upper atmosphere.

Atmospheric dynamic processes have been shown to be extremely complex and variable. The combination of accelerometer capabilities and orbital characteristics provides a unique opportunity to obtain new fundamental data. Long-term synoptic measurements anticipated from future flights coupled with the present results will provide a major contribution toward the goal of developing models that can accurately predict atmospheric behavior.

References

1. Marcos, F.A., McInerney, R.E., and Fioretti, R.W. (1978) Variability of the Lower Thermosphere Determined From Satellite Accelerometer Data, AFGL, Hanscom AFB, Mass., AFGL-TR-78-0134, ADA 058982.
2. Champion, K.S.W., and Marcos, F.A. (1973) The triaxial accelerometer system on Atmosphere Explorer, Radio Sci. 8:197.
3. Counts, J. (1975) Effects of Flexible Solar Arrays on Sensed Accelerations in a Rigid Spacecraft, VPI-E-75-13, Virginia Polytechnic Institute and State University, Blacksburg, Virginia.
4. Butler, T.A. (1977) Effect of Attitude Control Thruster-Induced Structural Vibrations on Sensed Accelerations of a Space Vehicle, Los Alamos Scientific Laboratories, Informal Report LA-6965-MS, Los Alamos, N.M.
5. Noonan, J.P., Fioretti, R.W., and Hass, B. (1975) Digital Filtering Analysis Applied to the Atmosphere Explorer-C Satellite MESA Accelerometer Data, AFCRL-TR-75-0293, ADA 015765.
6. Jacchia, L.G. (1971) Revised Static Models of the Thermosphere and Exosphere with Empirical Temperature Profiles, Spec. Rep. 332, Smithsonian Astrophys. Observ., Cambridge, Mass.
7. Sentman, L.H. (1961) Free Molecular Flow Theory and its Application to the Determination of Aerodynamic Forces, LMSC-448514, Lockheed Missiles and Space Co., Sunnyvale, Calif.
8. Mazzella, A.J., Jr. (1982) Drag Coefficients for a Satellite, AFGL Technical Report (in press).
9. Mazzella, A.J., Jr. (1982) Error Analysis for Densities and Winds, AFGL Technical Report (in press).
10. Kohl, H., and King, J.W. (1967) Atmospheric winds between 100 and 700 km and their effects on the ionosphere, J. Atmos. Terr. Phys. 29:1045.
11. Stern, D.P. (1978) Solar Terrestrial Programs: A Five Year Plan, NASA Goddard Space Flight Center, Greenbelt, Maryland.
12. Stern, D.P. (1977) Large-scale electric fields in the earth's magnetosphere, Rev. Geophys. Space Phys. 15:156.

13. Cole, K. D. (1962) Joule heating of the upper atmosphere, Aust. J. Phys. 15:223.
14. Straus, J. M., Creekmore, S. P., Harris, R. M., and Ching, B. K. (1975) Effects of heating at high latitudes on global thermospheric dynamics, J. Atmos. Terr. Phys. 37:1545.
15. Straus, J. M. (1978) Dynamics of the thermosphere at high latitudes, Rev. Geophys. Space Phys. 16:183.
16. Dickinson, R. E., Ridley, E. C., and Roble, R. G. (1981) A three-dimensional general circulation model of the thermosphere, J. Geophys. Res. 86:1499.
17. Forbes, J. M., and Marcos, F. A. (1979) Tidal variations in total mass density as derived from the AE-E MESA experiment, J. Geophys. Res. 84:31.
18. Forbes, J. M., and Marcos, F. A. (1980) Seasonal-latitudinal tidal structures of O, N₂, and total mass density in the thermosphere, J. Geophys. Res. 85:3489.
19. Forbes, J. M., and Garrett, H. B. (1979) Theoretical studies of atmospheric tides, Rev. Geophys. Space Phys. 17:1951.
20. Richmond, A. D., and Matsushita, S. (1975) Thermospheric response to a magnetospheric substorm, J. Geophys. Res. 80:2839.
21. Richmond, A. D. (1978) Gravity wave generation, propagation, and dissipation in the thermosphere, J. Geophys. Res. 83:4131.
22. Rice, C. J., and Sharp, L. R. (1977) Neutral atmospheric waves in the thermosphere and tropospheric weather systems, Geophys. Res. Lett. 4:315.
23. Chapman, R. D. (1977) Solar Terrestrial Programs: A Five Year Plan, NASA Goddard Space Flight Center, Greenbelt, Maryland.
24. Marcos, F. A., and Champion, K. S. W. (1979) Empirical model of lower thermospheric density for low solar flux and quiet geomagnetic conditions, Space. Res. 19:89.
25. Marcos, F. A., Garrett, H. B., Champion, K. S. W., and Forbes, J. M. (1977) Density variations in the lower thermosphere from analysis of the AE-C accelerometer measurements, Planet. Space Sci. 25:499.
26. Marcos, F. A., and Champion, K. S. W. (1979) Satellite Density Measurements with a Rotatable Calibration Accelerometer (ROCA), AFGL-TR-79-0005, ADA 069740.
27. Hedin, A. E., Salah, J. E., Evans, J. V., Reber, C. A., Newton, G. P., Spencer, N. W., Kayser, D. C., Alcayde, D., Bauer, P., Cogger, L., and McClure, J. P. (1977) A global thermospheric model based on mass spectrometer and incoherent scatter data, MSIS 1, N₂ density and temperature, J. Geophys. Res. 82:2139.
28. Forbes, J. M., Marcos, F. A., and Champion, K. S. W. (1978) Lower thermosphere response to geomagnetic activity, Space Res. 13:173.
29. Mayr, H. G., and Hedin, A. E. (1977) Significance of large-scale circulation in magnetic storm characteristics with applications to AE-C neutral composition data, J. Geophys. Res. 82:1227.
30. Mayr, H. G., Harris, I., and Spencer, N. W. (1978) Some properties of upper atmosphere dynamics, Rev. Geophys. Space Phys. 16:539.
31. Jacchia, L. G. (1977) Thermospheric Temperature, Density and Composition: New Models, Spec. Rep. 375, Smithsonian Astrophys. Observ., Cambridge, Mass.

32. Marcos, F.A., and Champion, K.S.W. (1972) Gravity waves observed in high latitude neutral density profiles, Space Res. 12:791.
33. Forbes, J.M., and Marcos, F.A. (1973) Thermospheric density variations associated with auroral electrojet activity, J. Geophys. Res. 78:3841.
34. Hanson, W.B., and Heelis, R.A. (1975) Techniques for measuring bulk gas motions from satellites, Space Sci. Instrum. 1:493.
35. Spencer, N.W., Niemann, H.B., and Carignan, G.R. (1973) The neutral-atmosphere temperature instrument, Radio Sci. 8:284.
36. Spencer, N.W., Theis, R.F., Wharton, L.E., and Carignan, G.R. (1976) Local vertical motions and kinetic temperature from AE-C as evidence for aurora-induced gravity waves, Geophys. Res. Lett. 3:313.
37. Nier, A.O., Potter, W.E., Hickman, D.R., and Maursberger, K. (1973) The open-source neutral mass spectrometer on Atmosphere Explorer-C, -D, and -E, Radio Sci. 8:271.
38. Knutson, J.R., Kayser, D.C., and Potter, W.E. (1977) Mass spectrometric measurement of thermospheric wind, J. Geophys. Res. 82:5253.
39. Hanson, W.B., Coley, N.R., and Heelis, R.A. (1980) Study of Upper Atmosphere Wind Motions, AFGL-TR-80-0307, ADA 097733.
40. Feess, W.A. (1973) Logacs Wind Analysis, USAF Rep. SAMSO-TR-73-355, Space and Missiles Systems Organization, Los Angeles, California.
41. Pearson, J.A. (1973) The Low-G Accelerometer Calibration System Orbital Accelerometer System, Rept. TR-0074(4260-10)-1, Aerospace Corp., Los Angeles, Calif.
42. DeVries, L.L. (1972) Analysis and interpretation of density data from the low-G accelerometer calibration system (LOGACS), Space Res. 12:777.
43. Wu, S.T., Matsushita, S., and DeVries, L.L. (1974) An analysis of the upper atmospheric wind observed by Logacs, Planet. Space Sci. 22:1036.
44. Hernandez, G., and Roble, R.G. (1976) Direct measurements of nighttime thermospheric winds and temperatures. 2. Geomagnetic storms. J. Geophys. Res. 82:5505-5511.
45. Evans, J.V. (1975) A review of F region dynamics, Rev. Geophys. Space Phys. 13:887.